SEDIMENTOLOGY the journal of the International Association of Sedimentologists

Sedimentology (2013) doi: 10.1111/sed.12049

Transferable wavelet method for grain-size distribution from images of sediment surfaces and thin sections, and other natural granular patterns

DANIEL BUSCOMBE[1]
School of Marine Science and Engineering, Plymouth University, Plymouth, Devon, UK
(E-mail: dbuscombe@usgs.gov)

ABSTRACT

In images of sedimentary or granular material, or simulations of binary (two-phase) granular media, in which the individual grains are resolved, the complete size distribution of apparent grain axes is well-approximated by the global power spectral density function derived using a Morlet wavelet. This approach overcomes many limitations of previous automated methods for estimating the grain-size distribution from images, all of which rely on either: identification and segmentation of individual grains; calibration and/or relatively large sample sizes. The new method presented here is tested using: (i) various types of simulations of two-phase media with a size distribution, with and without preferred orientation; (ii) 300 sample images drawn from 46 populations of sands and gravels from around the world, displaying a wide variability in origin (biogenic and mineralogical), size, surface texture and shape; (iii) petrographic thin section samples from nine populations of sedimentary rock; (iv) high-resolution scans of marine sediment cores; and (v) non-sedimentary natural granular patterns including sea ice and patterned ground. The grain-size distribution obtained is equivalent to the distribution of apparent intermediate grain diameters, grid by number style. For images containing sufficient well-resolved grains, root mean square errors are within tens of percent for percentiles across the entire grain-size distribution. As such, this method is the first of its type which is completely transferable, unmodified, without calibration, for both consolidated and unconsolidated sediment, isotropic and anisotropic two-phase media, and even non-sedimentary granular patterns. The success of the wavelet approach is due, in part, to it quantifying both spectral and spatial information from the sediment image simultaneously, something which no previously developed technique is able to do.

Keywords Grain size, granular patterns, sediment, texture analysis, wavelet analysis.

INTRODUCTION

Much insight can be gained from the grain-size distribution of granular materials, which are ubiquitous in the natural world. Measurements of deposited sediments have traditionally been hampered by: the intrusiveness of physical sampling; the expense of laboratory analyses of these samples; and, in some cases, the logistics of retrieval and transport which is especially the case for sub-aqueous or remote environments. Such information, automatically (and non-intrusively) obtained from photographs of such material provides a number of advantages over traditional forms of grain-size analysis, particularly in terms of money and time savings,

[1]Present Address: US Geological Survey, 2255 North Gemini Drive, Flagstaff, AZ, USA.

allowing much greater coverage and resolution compared to traditional laboratory methods, such as sieving and laser diffraction (Rubin, 2004; Barnard *et al.*, 2007). In dynamic environments, such as contemporary river beds, sea beds and aeolian sediment surfaces which are constantly changing under fluid power, robust automated image-processing techniques will, with minimal equipment, allow time-series of direct measurements of sediment properties for extended periods of time. This dense sampling might uncover physical processes/phenomena that traditional sampling, constrained by time and manual effort/expense in the field and subsequently in the laboratory, cannot (e.g. Paola & Seal, 1995; Mao *et al.*, 2011; Nelson *et al.*, 2012). In addition, dense spatial sampling from images taken in the field, or geo-rectified sediment imagery obtained from aerial (e.g. Carbonneau *et al.*, 2004, 2005) or even satellite platforms, will permit the creation of maps of sediment properties covering large continuous areas. It might even be possible to use similar techniques on hydro-acoustic images of lake, sea and river beds. For the above scenario to be a reality, techniques are required which are highly accurate and fully automated, and ideally which require no calibration.

Grain size has been estimated from photographs of sediment samples (with sufficient resolution such that individual grains can be identified by eye) for several decades (e.g. Kellerhals & Bray, 1971; Adams, 1979; Ibbeken & Schleyer, 1986; Butler *et al.*, 2001; Buscombe & Rubin, 2012b). If the physical sample is not required for laboratory-based analyses of physical and/or chemical properties of the sediment, automated analysis of sediment imagery is becoming a popular means by which to obtain dense measurements of grain size (e.g. Barnard *et al.*, 2007; Duller *et al.*, 2010; Gallagher *et al.*, 2011; Whittaker *et al.*, 2011; Baptista *et al.*, 2012).

Various methods have been reported which aim to provide robust and automated estimates of grain size from images, falling under two broad categories classified by Buscombe *et al.* (2010) as, respectively, 'geometrical' and 'statistical'. Both techniques require imagery where the smallest grains are resolved by at least a few pixels. Geometrical methods use image processing techniques (principally, thresholding and segmentation) to isolate and measure the visible axes (or portions of whole axes) of each individual grain (e.g. Graham *et al.*, 2005; Chang & Chung, 2012). In images of packed sediment, grains are touching with no apparent void space. The problem of touching and overlapping grains, and therefore no 'background' intensity against which to threshold, as well as the multifarious nature of sedimentary material, makes it difficult to design a universally applicable grain edge detection algorithm which works equally well for a wide range of sediment types (Buscombe *et al.*, 2010; Buscombe & Rubin, 2012b). If the segmentation algorithm is imperfect (i.e. if any grain is over-segmented or under-segmented, cf. Mao *et al.*, 2011) then errors accumulate non-linearly.

Statistical methods characterize grain size using a measure sensitive to image 'texture'. To date, these approaches have used autocorrelation (e.g. Rubin, 2004; Warrick *et al.*, 2009), semivariance (e.g. Carbonneau *et al.*, 2004, 2005) or one of several other methods, including fractals (e.g. Buscombe & Masselink, 2009) and grey-level co-occurrence matrices (e.g. Dugdale *et al.*, 2010). The statistical approach is substantially different from other forms of grain-size analysis, image-based or otherwise, because individual grains are not measured directly. One advantage of this approach is that success of the technique does not rely on successful identification, segmentation and sizing of each individual grain. However, all the above statistical methods require some form of calibration which tends to be site-specific or sediment-population specific. This prompted Buscombe *et al.* (2010) and Buscombe & Rubin (2012b) to propose generic expressions for, respectively, grain-size mean and standard deviation. Based on the information in the power spectrum of the image alone, moments of the grain-size distribution are estimated without resolving the entire distribution or measuring the individual grains directly. These estimations require neither calibration for a specific sediment type or geographic location, nor reliance on grain detection using advanced image processing; they therefore can be thought of as 'transferable' between sites.

A grey-scale (8-bit intensity) image of sediment can be treated as a continuous random field because the image is composed of numerous objects, with no correlation between grain location and grain colour, shape or size, and no 'background' intensity (Buscombe & Rubin, 2012b). As such, the image is described completely in a statistical sense by its mean and power spectrum (Buscombe, 2008; Buscombe *et al.*, 2010). Spectral analysis measures the strength of periodic components of the two-dimensional (2D) image intensities at different frequencies. The mean

grain size is related to a 'grain-scale' wave number, found to be associated with the offset at which the autocorrelogram of the image, R (autocorrelation as a function of pixel offset), falls to half its value at zero offset (Buscombe *et al.*, 2010). This estimate, grid by number style, is equivalent to the mean of all intermediate visible grain axes in the image. Due to resolution considerations, the physical area represented by a sample photograph is generally small compared to the scale over which deterministic structures in the sediment exist; however, this can be violated by grain-scale deterministic structure such as aligned/imbricated particles. If the sediment grains have a dominant preferred orientation then the technique may slightly over-estimate intermediate grain size, although to date this has not been quantified rigorously.

Buscombe & Rubin (2012b) provided experimental and numerical evidence that the shape of the radial average of a (2D) power spectral density function becomes less exponential with more grain-size fractions. This one-dimensional R was shown to be the normalized sum of the exponential decays in R corresponding to each of the grain sizes present. By quantifying the divergence in form between R from a sample image and R of an idealized material with the same mean but zero variance, an accurate measure of grain-size standard deviation can be derived, without having to measure the individual grains directly.

However, the statistical methods of Buscombe *et al.* (2010) and Buscombe & Rubin (2012b) only provide highly accurate estimates of grain-size mean and standard deviation (within a couple of tens of percent), not the full grain-size distribution, for relatively well-sorted sediment (grain size in a sample typically varying over 1 to 2 orders of magnitude). These methods are based on a Fourier approach which treats the image as though it is stationary (same mean, variances and range of frequencies throughout the image). However, this assumption is often violated, particularly when the image captures relatively small numbers of individual grains. Buscombe *et al.* (2010) suggested that there should be at least 1000 individual grains present in an image. Of course there might be fewer grains if the sediment is relatively coarse and the field of view relatively small, which could be particularly problematic for images of sedimentary thin-sections, and sediment cores which are narrow and in which grain size can change rapidly with depth.

Based on the above, it has become clear that neither the 'geometrical' nor the 'statistical' approach has been completely satisfactory, motivating the present study to develop an improved algorithm. If an image of a sediment bed is considered as a combination of both discrete (individual grains and their boundaries) and continuous (the randomness of grain placement and their surface variations) features, progress might therefore require a technique which merges the benefits of both geometrical and statistical approaches. Here, the continuous wavelet transform is explored and provides a basis for such a technique. The wavelet transform provides both spatial and spectral resolution which means that, whilst it is essentially a spectral method which decomposes an image of sediment into variance (or 'energy') as a function of frequency (related to statistical methods for quantifying grain size), importantly it also provides information on where peaks and troughs in energy occur, which could be used to identify the locations of individual grains.

Here, a new calibration-free (therefore transferable or 'universal'), conceptually simple method is proposed for accurate estimates of the entire grain-size distribution. It follows similar principles to Buscombe *et al.* (2010) and Buscombe & Rubin (2012b), treating an image of sediment or granular pattern as a random field, and then using spectral techniques to uncover the dominant spatial wavelengths within. The present method, however, adopts the wavelet-derived rather than Fourier-derived power spectrum.

Techniques based on the discrete wavelet and wavelet packet transform have long been used to classify images based on quantifying texture (e.g. Laine & Fan, 1993). Wavelet analysis has also proved useful in quantifying the orientation and length of pore networks in thin sections (Gaillot *et al.*, 1999) and pore networks in porous media (Qi & Neupauer, 2008, 2010). Here, it is demonstrated that the global wavelet power spectrum based on a Morlet mother wavelet provides an excellent calibration-free and transferable measure of grain-size distribution in images of natural sediment and other similar granular patterns. Because wavelet analysis does not require that the image is stationary or statistically homogeneous (Qi & Neupauer, 2008), the present technique, compared to previous methods, is less sensitive to the absolute number of grains present; more applicable for poorly sorted sediments (grain size in an individual image/sample typically varying over ≥ 2 orders of magnitude), less sensitive to any preferred orientation of grains in the image and applicable to

images of sediment with and without an apparent void fraction (pore spaces between grains).

METHOD

The spatial distribution of pixel intensity in an image of sediment (Fig. 1A and B) is a continuous random field (Buscombe *et al.*, 2010) and, as such, the power spectral density simultaneously captures information on all scales of variability. These scales are associated with different grain sizes, but also image noise and any scale associated with light and shadows greater than the grain scale.

Wavelet transforms provide a mathematically robust and unified framework for multi-scalar scale analysis. The signal is decomposed using a series of functions (wavelets) created by scaling and translation of a base function called the mother wavelet. The wavelet transform is defined as the convolution of discrete sequence y_n ($n = 0, \ldots, N-1$ sampled at equal spacing, δy, i.e. each pixel), where y denotes the long dimension of the image, with a scaled and translated version of a normalized mother wavelet function ψ_0, in one dimension given by (Torrence & Compo, 1998):

$$W_n(s) = \sqrt{\frac{\delta y}{s}} \sum_{n'=0}^{N-1} y_{n'} \psi_0^* \left[\frac{(n'-n)\delta y}{s} \right] \qquad (1)$$

where δy is the spacing in y_n (i.e. one pixel), the apostrophe indicates transpose and the asterisk symbolizes complex conjugate. By varying the scale, s, and translating in location, n, a 1D series is expressed in a 2D parameter space (n, s). This 2D parameter space, sometimes called a scalogram, is computed by setting the scale (s) to a constant value and solving across all location values (n), then repeating for all scales. These scales can be specified. Here, scales less than three pixels were not considered, nor were scales greater than a third of the greatest dimension of the image. The complex-valued Morlet wavelet is adopted as the mother wavelet, defined as:

$$\psi_0(\eta) = \pi^{-\frac{1}{4}} e^{i\omega_0 \eta} e^{-\eta^2/2} \qquad (2)$$

where i is the imaginary unit, non-dimensional frequency ω_0 is 6 and η is dimensionless space such that the wavelet is stretched by varying. The $\sqrt{\delta y/s}$ term in Eq. 1 ensures that the wavelet transform is weighted by y_n only, and not by Eq. 2. The Morlet is adopted because different spatial scales are uncorrelated (Laine & Fan, 1993), and because it is very well-resolved in both the spatial and frequency domains (in the spatial domain, it has ω_0 peaks in a relatively narrow band, and a single peak in the frequency domain – the reader is referred to Torrence & Compo (1998) for more details). Being a non-orthogonal wavelet, it does not spuriously count the power contribution of certain frequencies (Farge, 1992), and therefore the power spectrum has peaks, at accurate frequencies, roughly proportional to the squared amplitudes of the signal (cf. Grinsted *et al.*, 2004).

Prior to analysis, the image is zero-padded to the next power of 2 greater than N, the largest dimension of the image. No image filtering is required. The wavelet transform Eq. 1 is calculated for a representative selection of y_n, both rows and columns. Typically, the analyses performed here utilized one half or one third of rows and the same proportion of columns. For each y_n, the linear trend is removed and the wavelet transform is computed using Eq. 1. When wavelet transforms have been computed for all y_n, the global wavelet power spectrum is calculated, given by:

$$\bar{W}^2 = \frac{1}{N} \sum_{n=0}^{N-1} |W_n(s)|^2 \qquad (3)$$

The spectrum is called 'global' because it averages over location, retaining information only on the scale. The global wavelet spectrum provides an unbiased and consistent estimate of the true power spectrum of a spatial-series (Percival, 1995). The analysis may be carried out in 2D (e.g. Qi & Neupauer, 2010); however, for simplicity, here the average of spectra from simpler 1D transects through the image was used.

The radial average of the Fourier-derived power spectral density (calculated using a standard Fast Fourier Transform approach, or FFT, according to Buscombe & Rubin, 2012b) tends to show large energy at scales smaller than grains, suggesting over-sensitivity to small-wavelength variations in image intensity associated with noise and intra-granular variations (for example, surface texture of individual grains). In addition, any directionality or non-diffusivity in the lighting causes disproportionately large energy at scales larger than those at the grain scale.

The above is illustrated by analysis of an image of well-sorted oolitic sediment from a

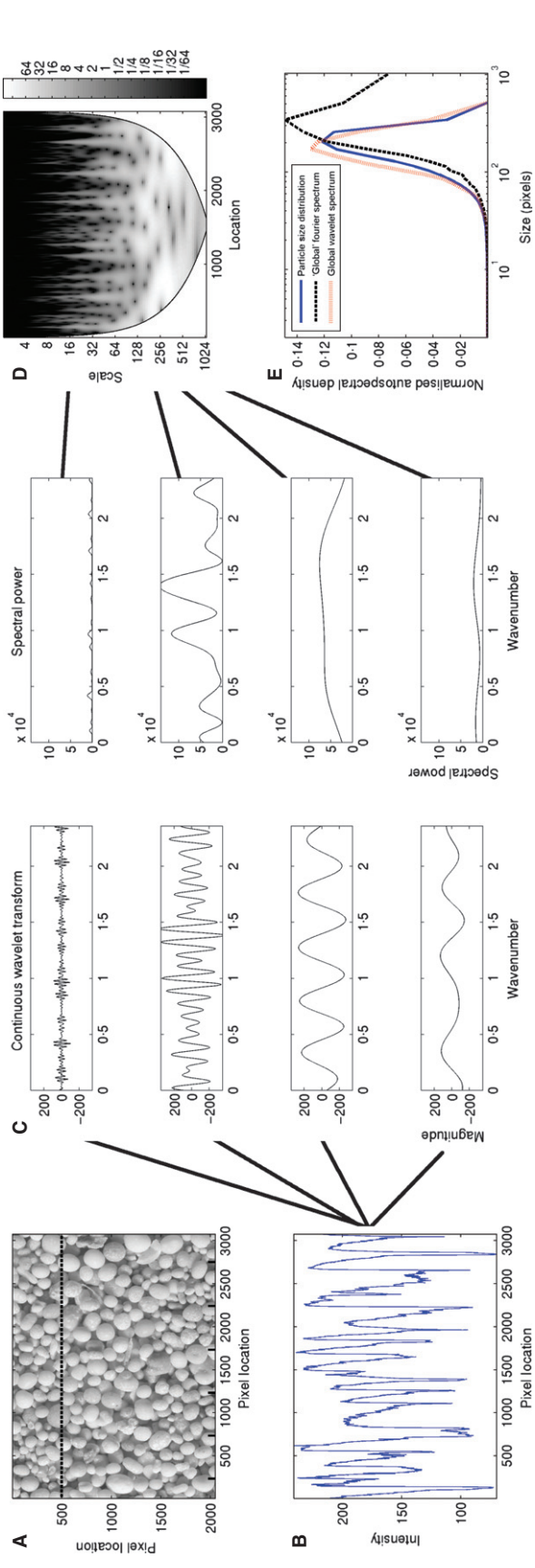

Fig. 1. (A) Image of a simple sediment composed of well-sorted ooids. The ticks at the base of the image are separated by 1 mm. (B) The intensity trace through one row of the image. The location is marked by the dashed line in (A). (C) The continuous wavelet transforms (left) for a selection of scales (going down the page), and their associated power spectra (right). (D) The continuous wavelet transform of the data in (B). The shading corresponds to spectral power given by the colour bar. The vertical axis is the scale in pixels and the horizontal axis is pixel location. (E) The grain-size distribution of intermediate axes measured on-screen (heavy line), the mean of Fourier-derived autospectra for each line of image (A), normalized by the sum (dashed line) and the normalized wavelet-derived global power spectrum (dotted line).

beach in the Bahamas (Fig. 1A). One row of pixel values (Fig. 1B) serves to illustrate the treatment of image intensity as a continuous random variable. At each scale, the continuous wavelet transform (Fig. 1C, left plots) is used to compute the power spectrum at that scale (Fig. 1C, right plots). The wavelet transform of the data at each scale (Fig. 1C, left) is computed as a convolution of the data (Fig. 1B) and a scaled and translated mother wavelet. The power spectrum (Fig. 1C, right) is the squared amplitudes of the wavelet transformed data. This information is compiled for each scale, and shown as the full continuous wavelet transform of the data in Fig. 1B, depicted in Fig. 1D, which shows spectral power (shade) as a function of scale (wavelength) and pixel location along the data series. Scales and locations where there is low spectral power (few grains with that wavelength) are dark. Light areas correspond to grain wavelengths with high spectral power (large number of grains with that wavelength). The blanked-out peripheral area of the spectrum in Fig. 1D is known as the 'cone of influence' (COI), and is the portion of the spectrum sensitive to end-effects, calculated according to Grinsted *et al.* (2004). Spectral power outside the COI tends to peak at a scale around 100 to 300 pixels. If this wavelet spectrum is calculated for a representative number of rows and columns through the image in Fig. 1A, and averaged in location, then these 1D spectra averaged again, this produces the 'global' wavelet spectrum Eq. 3 which is the dotted line in Fig. 1E in normalized form. The grain-size distribution compiled from intermediate diameters of grains measured manually on the image (Fig. 1E, solid line), following the method of Barnard *et al.* (2007), again normalized to sum to unity, is well-approximated by the wavelet-derived global power spectrum but not the normalized Fourier-derived power spectrum (Fig. 1E, dashed line). The Fourier-derived spectrum contains a significant amount of energy associated with large wavelengths due to aliasing. The wavelet-derived spectrum, in contrast, will consistently taper to zero energy at these wavelengths which are much greater than any grain scale.

Wavelet analysis is a more powerful method for sediment images than a Fourier analysis based on the windowed FFT for two principal reasons. Firstly, it averages over both space and frequency which allows it to circumnavigate the strict stationarity requirement of Fourier-based spectral estimation. Secondly, frequency resolution is constant over frequency, whereas in a FFT analysis frequency resolution decreases with increasing frequency (Farge, 1992), meaning that the small wavelengths cannot be well-resolved. The two issues are related: the windowed FFT computes a handful of individual spectra over the data. The larger the spatial window used, the better the frequency resolution of the spectra. However, improved frequency resolution is achieved by reducing spatial resolution. In a global wavelet transform, this compromise is, in effect, avoided. The continuous wavelet transform does not window across the data and therefore provides a better spatial resolution, at the expense of relatively poor frequency resolution at very high frequencies. In the case of traces of intensity in sediment images, these high frequencies will almost always be intra-grain scale 'noise' in a well-resolved image of sediment where grains are covered by several pixels. Both spectral and spatial information is being heavily averaged in such an approach, rather than one or other being discarded which occurs in geometrical (image-processing based) and Fourier-based approaches to grain size from images.

If the global wavelet power spectrum is a non-biased estimate of the variance contributions of grain-scale wavelengths within an image of sediment then, where $P(d)$ is distribution of grain sizes $d = 1/\pi s$ (where s is the wavelet scale, normalized such that $\Sigma P(d) = 1$) in an image composed wholly of grains with no interstices or 'background' intensities:

$$P(d) \approx \frac{\bar{W}^2}{\sum \bar{W}^2} \tag{4}$$

For the spectrum to be non-biased, and in order for the variance at the wavelength of the individual grain(s) to be large, the image intensities across individual grains must be more slowly varying and larger (brighter) than the abrupt and smaller (darker) intensity differences between grains (in interstices).

WAVELET SPECTRA OF SOME IDEALIZED CASES

To test the above method, wavelet analysis was carried out on some idealized binary simulated image of granular material. Similar simulations were used by Buscombe *et al.* (2010) and Buscombe & Rubin (2012a) to explore the limits and sensitivities of automated image-based

grain-size techniques, because it is relatively simple to control grain size, shape, apparent porosity and other attributes of sediments independently.

Simulated images were composed of either spheres or ellipses possessing a log-normal size distribution with an equal mean (μ) and standard deviation (σ). Grain size and position were independent. The images were generated using the algorithms detailed in Tschopp *et al.* (2008). The distributions of particle major axes were identical for each set of images composed of circles (Fig. 2) or ellipses (Fig. 3), leaving only the areal void fraction, ϕ (in these cases, the proportion of pixels with value 0), to vary. For the cases using elliptical particles, the major axis length was always twice the minor axis length. Void pixels are zero-valued, and thus contain no spectral power, which means the method given by Eq. 4 must be slightly modified to factor in only the areal proportion of the image covered by grains, therefore grain sizes are given by $d = (1/\pi\phi)s$.

The root mean square (RMS) error, Ψ, and mean absolute error, M, between a measured, q_{meas}, and estimated, q_{est}, quantity (both of length n) was computed for a selection of commonly used distribution percentiles, P_m (where m symbolizes percentile). Mean absolute and RMS errors are given by, respectively:

$$\Psi = \frac{\sqrt{\sum \left(q^i_{\mathrm{meas}} - q^i_{\mathrm{est}}\right)^2}}{n} \tag{5}$$

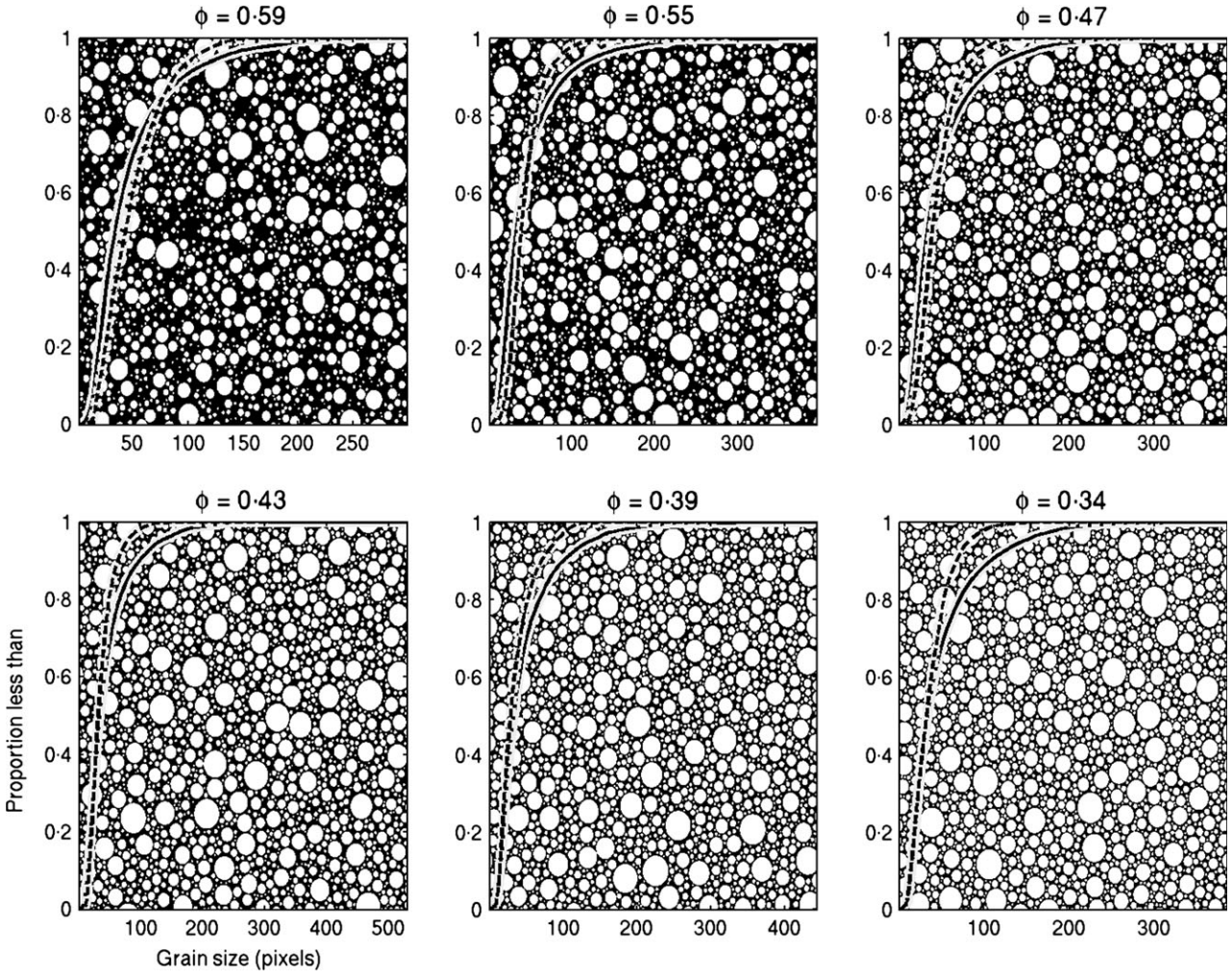

Fig. 2. Simulated two-phase media (white areas are particles, black areas are void spaces) consisting of circles, along with their known particle size distributions (continuous lines) and estimated size distributions (dashed lines). In each subplot, the horizontal axis is grain size in pixels and the vertical axis is proportion less than. The title of each subplot is the void fraction of the simulation underneath. Error statistics for these samples are presented in Table 1.

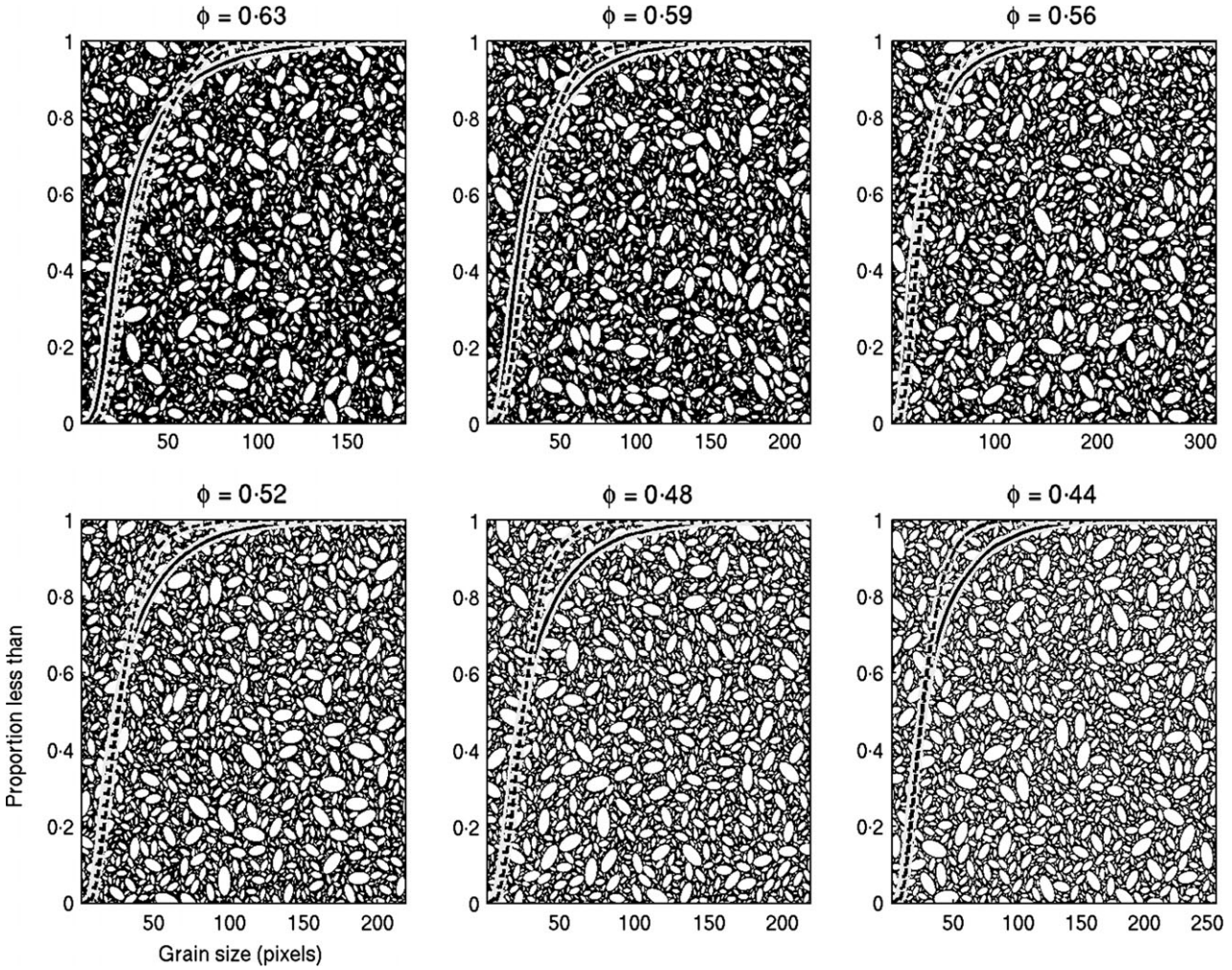

Fig. 3. Simulated two-phase media (white areas are particles, black areas are void spaces) consisting of ellipses (the major axis is always twice the minor axis length), along with their known particle size distributions (continuous lines) and estimated size distributions (dashed lines). In each subplot, the horizontal axis is grain size in pixels and the vertical axis is proportion less than. The title of each subplot is the void fraction of the simulation underneath. Error statistics for these samples are presented in Table 2.

and:

$$M = \frac{1}{n}\sum\left(|q^i_{\text{meas}} - q^i_{\text{est}}|\right) \tag{6}$$

In addition, to aid comparisons with previous studies (such as Graham *et al.*, 2005; Warrick *et al.*, 2009; Buscombe *et al.*, 2010), the irreducible random error was calculated, defined as the RMS error that cannot be accounted for by the mean absolute error and given by (Graham *et al.*, 2005):

$$e_i = \sqrt{\psi^2 - M^2} \tag{7}$$

The agreement was reasonably good, as illustrated graphically by comparing the solid and dashed lines in Figs 2 and 3 which show, respectively, the measured and estimated particle size distributions overlying the images. The errors are reported in Table 1 for the spherical particle simulations and in Table 2 for the elliptical particle simulations. Discrepancies were uncorrelated with ϕ and, in general, were larger for the tails of the distribution than for the central percentiles, which is to be expected because the sample size of those particles in the tails of the size distribution is smaller. Errors were generally smaller for the images composed of elliptical particles (e_i of around 10% compared to 12 to 18% for the spherical particles) probably because the absolute number of particles in those images (between 2448 and 3320, depending on ϕ) was greater than for the images composed of spheres

Table 1. Error in percentile estimates for the log-normal binary spheres (μ = 47 pixels, σ = 40 pixels). Units are pixels. Values in parentheses have been normalized by the particle size associated with that percentile, and multiplied by 100 to give a percent error.

Percentile	P_{10}	P_{16}	P_{25}	P_{50}	P_{75}	P_{84}
Ψ	4·35 (29%)	5·34 (31%)	6·25 (31%)	6·87 (23%)	6·97 (15%)	10·83 (19%)
M	3·71 (25%)	4·39 (26%)	5·02 (25%)	5·93 (20%)	5·23 (11%)	8·39 (15%)
e_i	2·28 (15%)	3·03 (18%)	3·73 (18%)	4·60 (12%)	4·60 (10%)	6·84 (12%)

Table 2. Error in percentile estimates for the log-normal binary ellipses (μ = 34 pixels, σ = 26 pixels). Units are pixels. Values in parentheses have been normalized by the particle size associated with that percentile and multiplied by 100 to give a percent error.

Percentile	P_{10}	P_{16}	P_{25}	P_{50}	P_{75}	P_{84}
Ψ	2·73 (24%)	3·13 (23%)	3·54 (22%)	3·70 (15%)	5·31 (13%)	10·31 (19%)
M	2·44 (21%)	2·81 (21%)	3·22 (20%)	2·94 (12%)	4·52 (11%)	8·42 (16%)
e_i	1·24 (11%)	1·38 (10%)	1·47 (9%)	2·25 (9%)	2·81 (7%)	5·94 (11%)

(between 1427 and 2132, depending on ϕ), owing to the generally smaller grain size.

NATURAL SEDIMENT SAMPLES

The above analysis of idealized sediments demonstrates that the wavelet method is suitable for images composed of regularly and identically shaped non-touching, non-overlapping particles (possessing a log-normal size distribution) separated by voids. The errors are small even though each image was composed of relatively small absolute numbers of particles (between *ca* 1500 and 3000). In this section, the same method is tested on images of natural sediments which are non-uniform in shape, touching or overlapping with no apparent void fraction, and non-uniform in shading (both between and within individual grains).

The wavelet method Eq. 4 was tested using three sets of images summarized in Table 3. Set A is a collection of 262 digital photographs of samples representing eight distinct sedimentary populations. The collection is the same as that used by Buscombe & Rubin (2012b) and contains images of sand and gravel sediments from beaches, rivers and continental shelves. An example image from each of the eight populations is shown in Fig. 4 (one population is represented twice – subplots a and c – so there are nine images in Fig. 4). Each of the eight populations was collected with a different imaging system.

Table 3. Summary of data sets used to test the wavelet method.

	Number of sample images and sediment populations	Description
Set A	262 (drawn from eight populations)	Unconsolidated sands/gravels, different imaging system per population
Set B	9 (one from each population)	Thin sections of sandstones, same imaging system per population
Set C	38 samples (one from each population)	Unconsolidated sands/gravels, same imaging system per population

The size distribution of intermediate axes of apparent (surface) grains was compiled for each image following the on-screen manual method of Barnard *et al.* (2007). This time-consuming process is the only way in which to reliably obtain a comparable grain-size distribution to that provided by image-based methods (Warrick *et al.*, 2009; Buscombe *et al.*, 2010; Baptista *et al.*, 2012).

The method was also tested using a collection of digital photographs of petrographic thin section samples from sedimentary rocks, named set

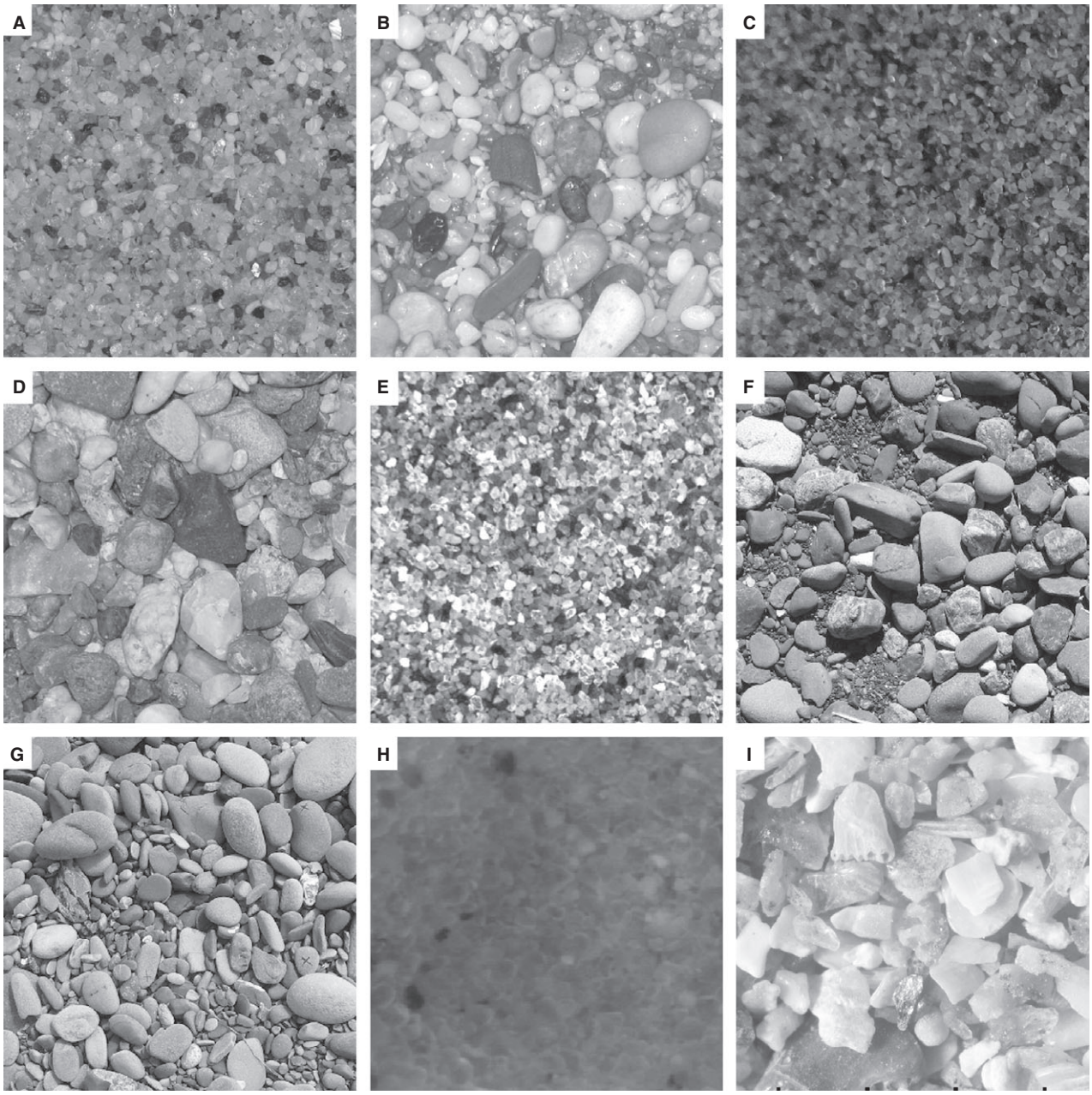

Fig. 4. Example sample images from set A: the populations of natural beach, river and continental shelf sediments tested, as listed in Table 3. The current technique is equally applicable, unmodified, to all of these sediment types.

B (Fig. 5). The major differences between the sediment surface images and the thin section images are the pore space and the non-overlapping grains with no relief. The apparent grain-size distribution was measured from the nine section images in the same way as above. To estimate ϕ, a simple threshold was applied to each image which counted as void any pixel with an intensity value less than the 5% value of the cumulative distribution of all pixel values for that image.

Finally, the method was tested using another set of images of unconsolidated sand and gravel sized sediments, named set C (Fig. 6). Compared to set A, images in set C were characterized by generally fewer individual grains. In most images, there were much fewer than 1000 grains, the number suggested by Buscombe *et al.* (2010) to be the lower limit on sample size for their method for grain size based on the Fourier-derived spectrum of the image. Set C also contained a larger

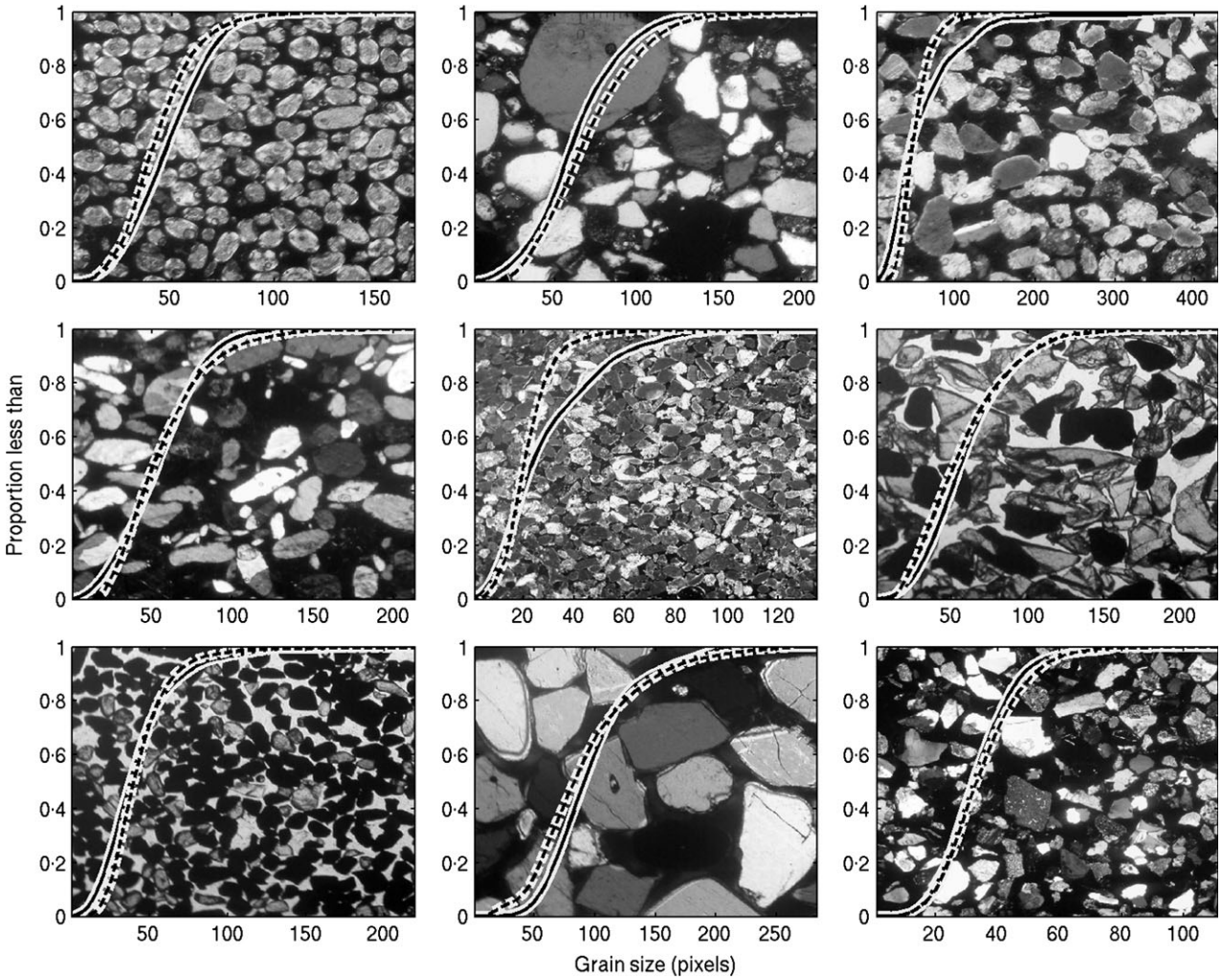

Fig. 5. Square portions of images of nine petrographic thin sections (set B), along with their known particle size distributions (continuous lines) and estimated size distributions (dashed lines). In each subplot, the horizontal axis is grain size in pixels and the vertical axis is proportion less than. Error statistics for these samples are presented in Table 4.

diversity of sediment types represented (biogenic and mineralogical, including many volcanic sands and gravels) and their characteristic surface textures and distributions of shape. Images in set C were all taken with the same imaging equipment (handheld digital camera and controlled indoor lighting). Once again the apparent grain-size distributions were compiled using the on-screen manual 'point-counting' method.

In all of the images in sets A to C, the smallest grains are resolved by a few pixels, and the outlines of these grains are seen under zoom. In each case, the image plane was parallel with the object plane, or as close as not to matter, therefore no orthorectification was required. The images were not affected significantly by distortion (barrel or pincushion). Therefore, the spatial resolution of the image (unit length/pixel) was taken to be constant over the entire image. All values are reported in pixels, but unit length is obtained by multiplying by a spatial resolution (length/pixel). If, however, distortion is present and/or images were not taken parallel to the surface, the image would have to be corrected and/or orthorectified prior to use.

RESULTS

Images of natural sands and gravels (large sample size: set A)

Six commonly utilized percentiles of the cumulative size distribution (namely 10, 16, 25, 50, 75

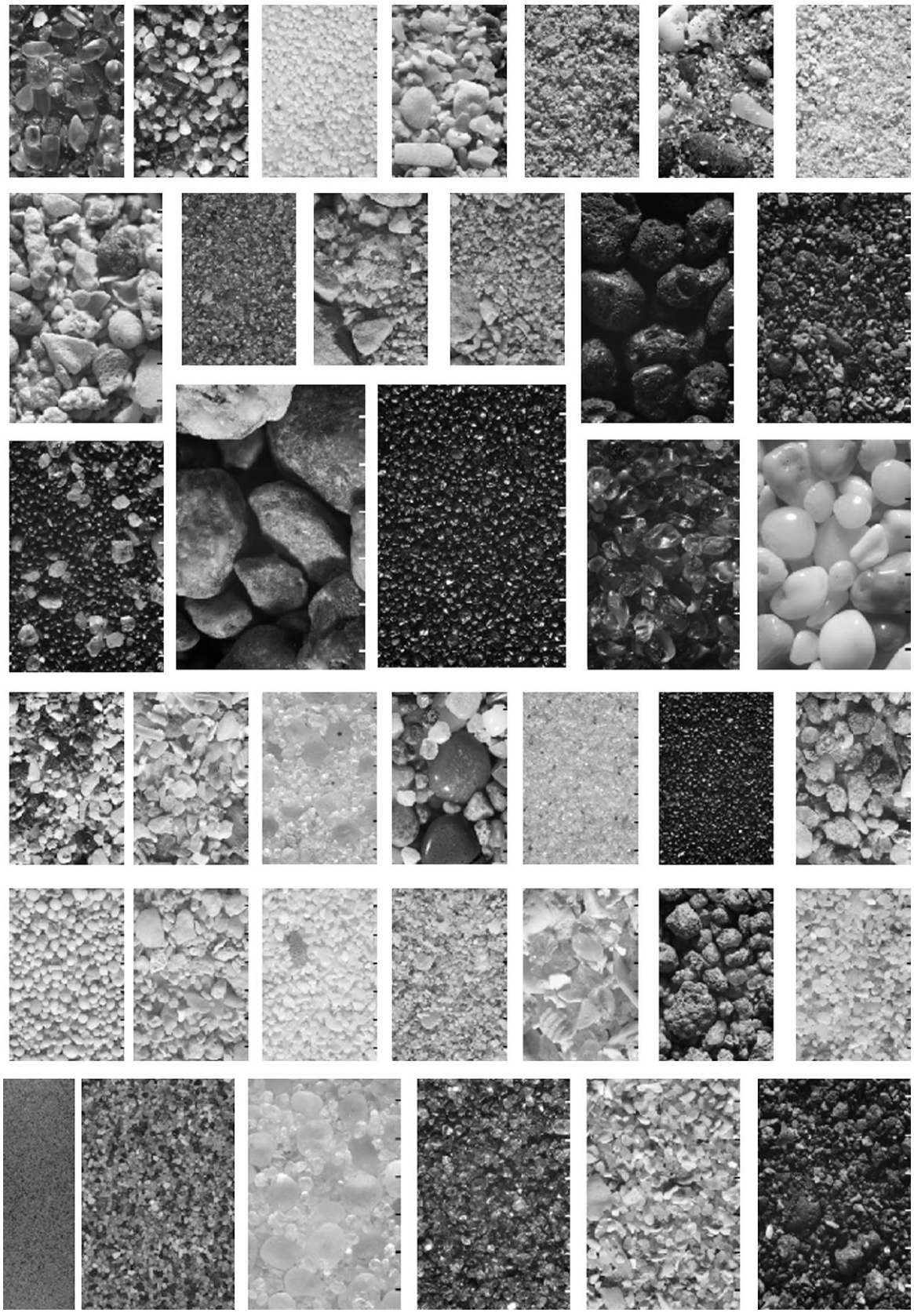

Fig. 6. Example sample images from the populations of natural sediments with relatively small number of individual grains, set C, as listed in Table 3. The tick marks on these images are 1 mm apart.

and 84) were calculated for each measured and estimated size distribution. The agreement for each percentile, quantified by ψ values between 14% and 37%, is very good (Fig. 7) and mean sizes are comparable to the previous method of Buscombe *et al.* (2010). Error statistics per percentile are summarized in Table 4. There is a slight negative bias up to the 50th percentile where the algorithm consistently slightly underestimates grain size. This is probably due to the algorithm being more sensitive to few numbers of the smallest grains than few numbers of the largest grains, which would perhaps explain why the bias decreases with percentile. Such bias can be corrected for, for a given population, by carrying out point counts on images of a few end members of the grain-size spectrum for that population (see Buscombe *et al.*, 2010). The same error metrics have been computed for the 10th, 50th and 84th percentile results of Buscombe (2008), a Fourier-based spectral method for grain-size distribution estimates (Table 5). Errors using that method are larger than the present method (Table 4) for the coarse percentiles, and comparable for the fine and median percentiles. The method of Buscombe (2008)

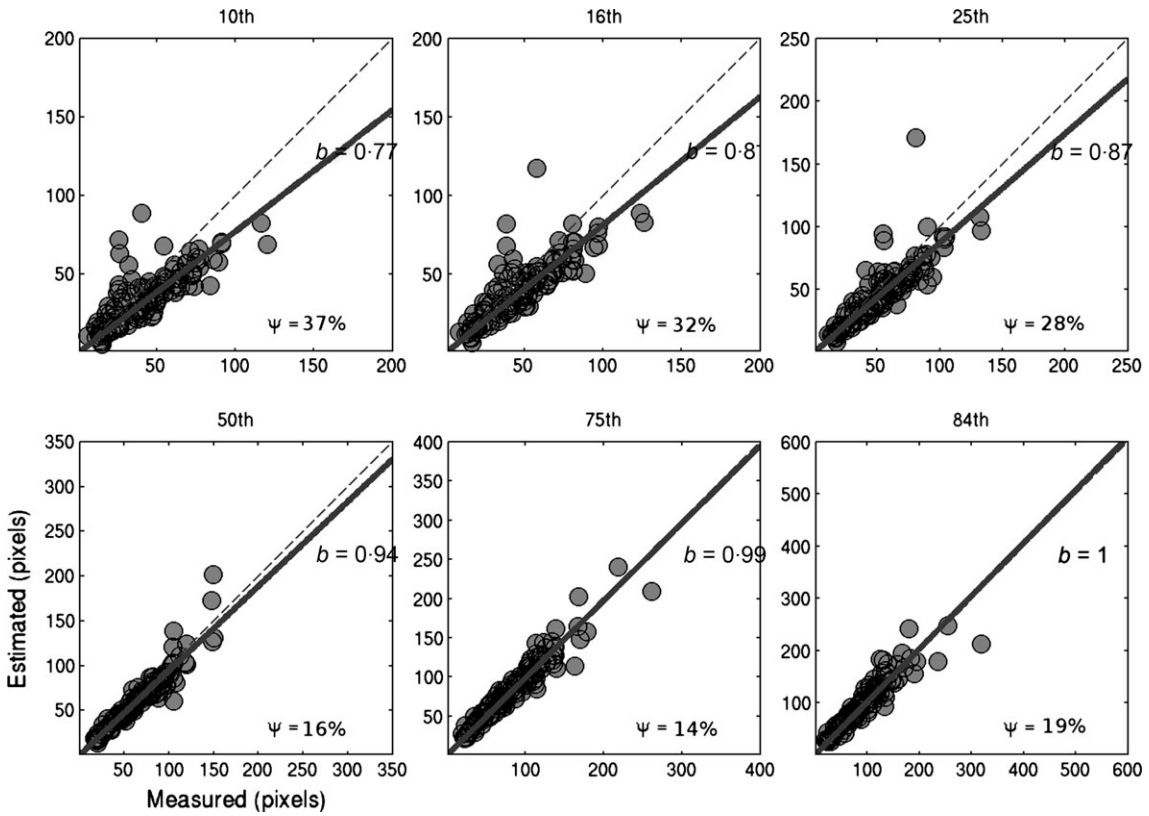

Fig. 7. Measured (horizontal axes) versus estimated (vertical axes) grain-size distribution percentiles from the samples in set A (Fig. 4). Subplots from left to right and top to bottom are the 10th, 16th, 25th, 50th, 75th and 84th percentiles. In each subplot, the dashed line is the 1:1 relation and the solid line is the linear least squares fit. The slopes of those lines (b) and the normalized root mean square error (ψ) are shown for each percentile. Error statistics for these samples are presented in Table 5.

Table 4. Error in aggregated percentile estimates for set A. Units are pixels. Values in parentheses have been normalized by the mean particle size associated with that percentile and multiplied by 100 to give a percent error.

Percentile	P_{10}	P_{16}	P_{25}	P_{50}	P_{75}	P_{84}
Ψ	15·77 (37%)	15·17 (32%)	14·86 (28%)	10·77 (16%)	11·92 (14%)	18·61 (19%)
M	12·49 (29%)	11·71 (25%)	10·58 (19%)	7·20 (11%)	8·46 (10%)	12·36 (13%)
e_i	9·61 (22%)	9·64 (20%)	10·43 (19%)	8·01 (11%)	8·39 (9%)	13·92 (14%)

Table 5. Error in aggregated 10th, 50th and 84th percentile estimates obtained by Buscombe (2008) for a similar method which relied on calibration, based on one population analysed. Units are millimetres. Values in parentheses have been normalized by the mean particle size associated with that percentile and multiplied by 100 to give a percent error.

Percentile	P_{10}	P_{50}	P_{84}
Ψ	0·40 (25%)	0·45 (17%)	2·40 (35%)
M	0·28 (17%)	0·39 (15%)	1·98 (29%)
e_i	0·28 (18%)	0·23 (9%)	1·37 (20%)

requires calibration for each site/sediment type and was validated using only one sedimentological population (well-sorted fine gravels).

Thin section images of sedimentary rocks (set B)

Figure 5 shows grey-scale images of the nine example petrographic thin sections of consolidated sediments with apparent pore space, along with their measured (solid lines) and estimated (dashed lines) size distributions. The agreement between measured and estimated distribution percentiles (Fig. 8) is good, with ψ ranging between 9·5% and 28%. The errors are, as expected, largest for the percentiles near the tails of the distributions owing to the relatively small sample numbers. Error statistics per percentile are summarized in Table 6. In this case, computed biases are very small for all percentiles, probably owing to the very low level of small-wavelength noise in the sample images.

Images of natural sediments (small sample size: set C)

Analysis using images from set C, which all have few numbers of grains (tens to hundreds), reveals that RMS error is found to go approximately inversely with sample size (number of grains per image), for all percentiles of the distribution. Some examples of images within set C with larger numbers of grains (more than 200) are shown in Fig. 9 along with measured (solid)

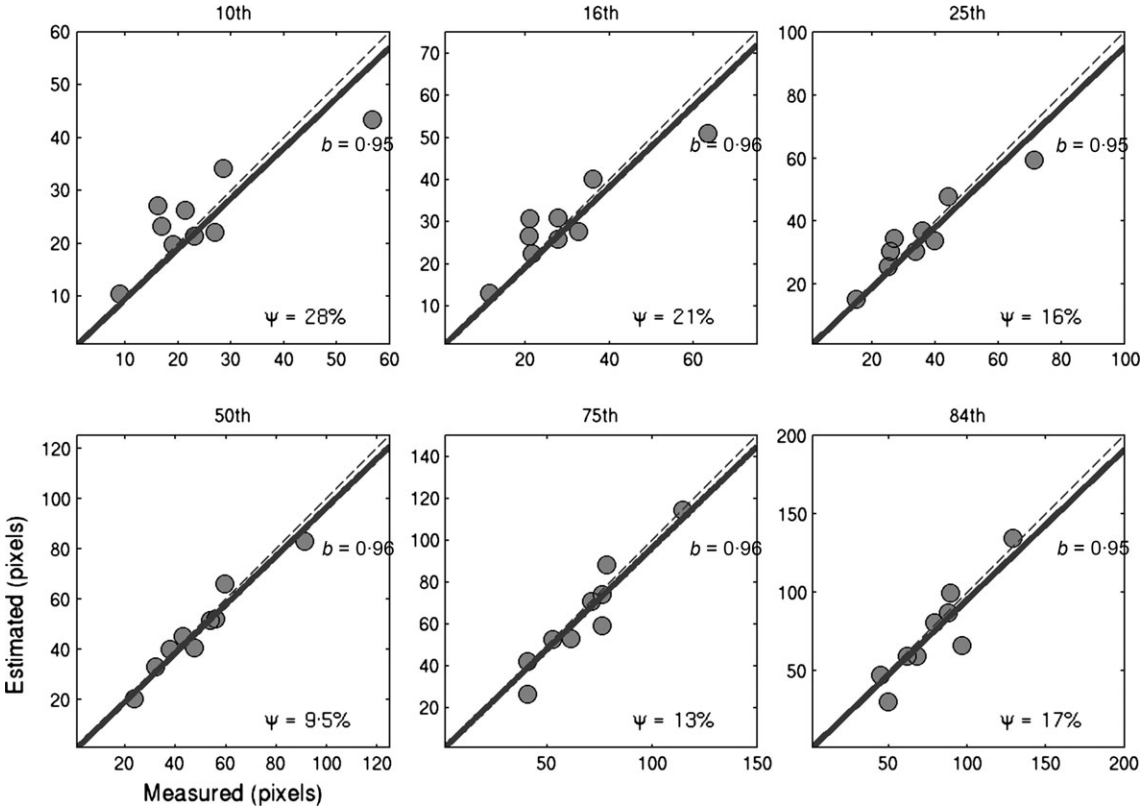

Fig. 8. Measured (horizontal axes) versus estimated (vertical axes) grain-size distribution percentiles from the samples in set B (Fig. 5). Subplots from left to right and top to bottom are the 10th, 16th, 25th, 50th, 75th and 84th percentiles. In each subplot, the dashed line is the 1:1 relation and the solid line is the linear least squares fit. The slopes of those lines (b) and the normalized root mean square error (ψ) are shown for each percentile.

Table 6. Error in aggregated percentile estimates for set B. Units are pixels. Values in parentheses have been normalized by the mean particle size associated with that percentile and multiplied by 100 to give a percent error.

Percentile	P_{10}	P_{16}	P_{25}	P_{50}	P_{75}	P_{84}
Ψ	6·84 (28%)	6·13 (21%)	5·59 (16%)	4·67 (9·5%)	8·49 (13%)	13·02 (17%)
M	5·58 (23%)	4·92 (16%)	4·38 (12%)	4·02 (8%)	5·89 (9%)	9·03 (11%)
e_i	3·96 (16%)	3·65 (12%)	3·47 (9%)	2·38 (5%)	6·11 (9%)	9·38 (12%)

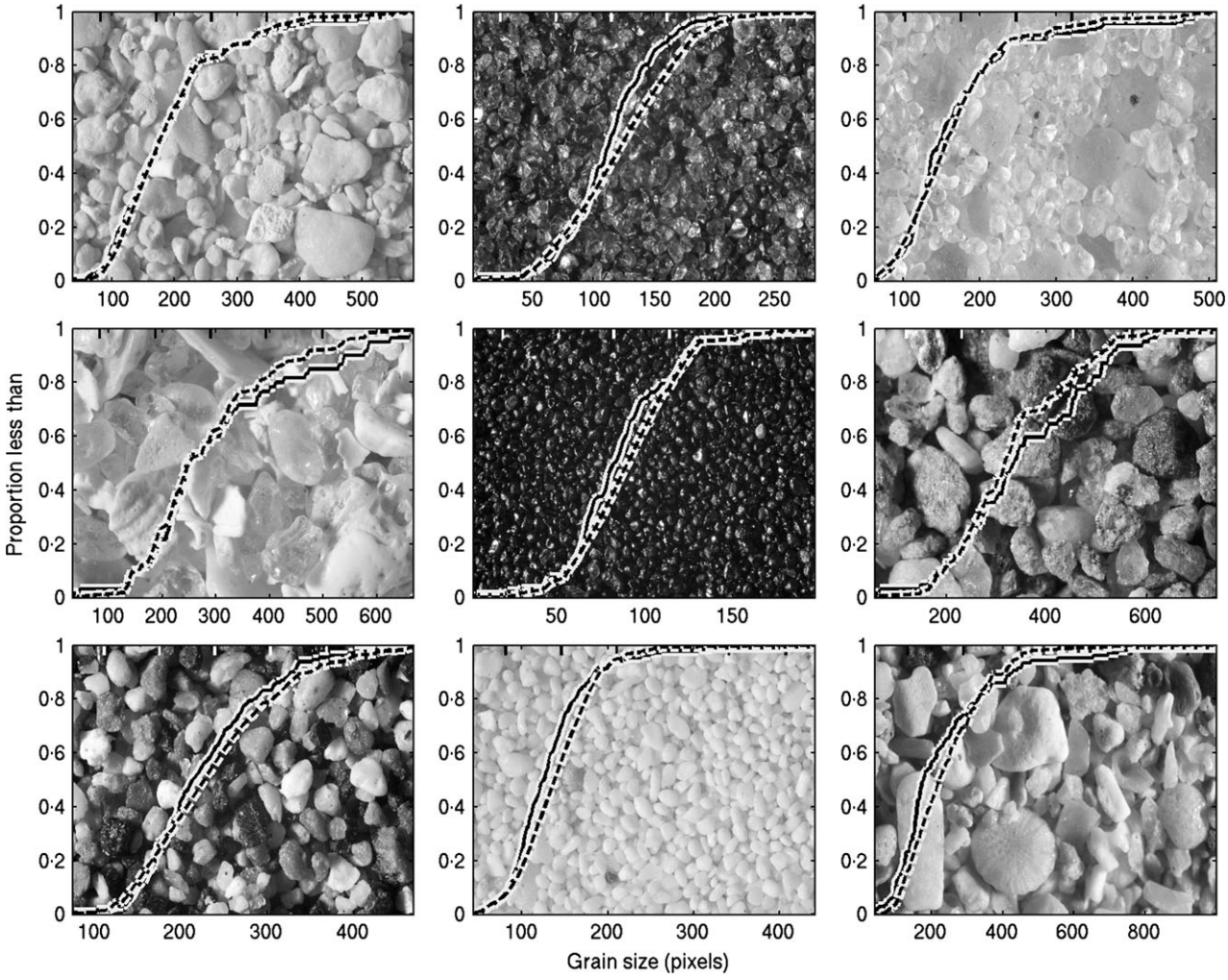

Fig. 9. Square portions of nine of the samples depicted in Fig. 6, along with their known particle size distributions (continuous lines) and estimated size distributions (dashed lines). In each subplot, the horizontal axis is grain size in pixels and the vertical axis is proportion less than. These are examples where the grain-size algorithm has worked well, despite the small number of individual grains.

and estimated (dashed) cumulative grain-size curves. These samples have RMS errors of less than 50% for all percentiles computed. Figure 10, in contrast, depicts some sample images where the wavelet method yielded particularly poor estimates. These include samples with very few numbers of grains (for example, top middle and bottom right), and also examples where the intensity variations between grains is limited (top left, bottom middle), which also yields relatively poor predictions. Together, Figs 9 and 10 serve to visually illustrate the skill and limits of the new method in terms of sample size and sedimentological variability.

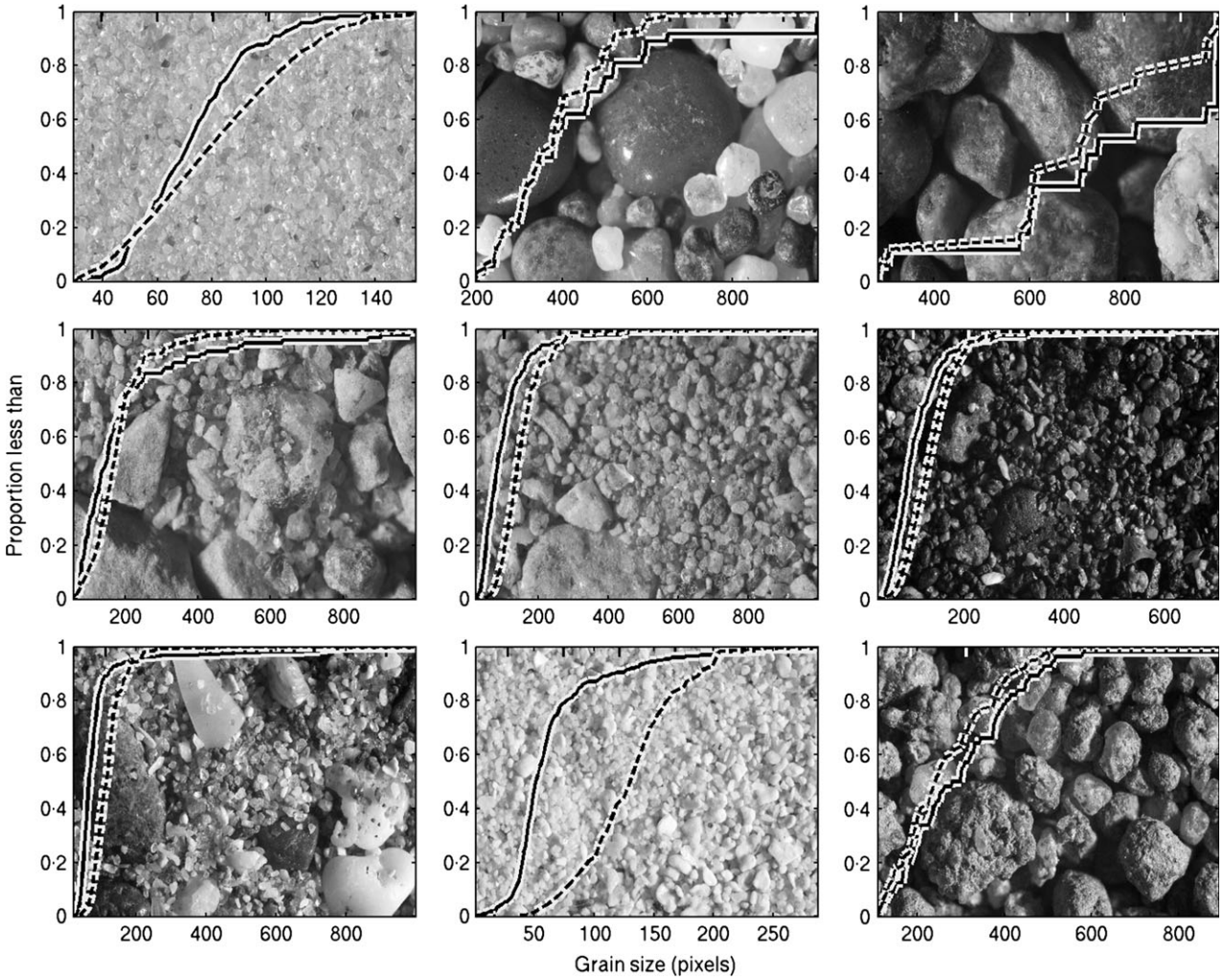

Fig. 10. Square portions of nine of the samples depicted in Figure 6, along with their known particle size distributions (continuous lines) and estimated size distributions (dashed lines). In each subplot, the horizontal axis is grain size in pixels and the vertical axis is proportion less than. These are examples where the grain-size algorithm has not worked well (the reasons for which are discussed in the text).

Images of sedimentary cores

This approach could also be useful for images of cores through deposits. Often sediment cores show considerably greater sedimentological variability than a given sample of a sedimentary rock or unconsolidated sediment accessible from the surface. However, the narrowness of cores could limit use of the methods of Buscombe *et al.* (2010) or Buscombe & Rubin (2012b) because of the small sample size. The new method was applied to a number of high-resolution scans of cores taken as part of the Integrated Ocean Drilling Program (Mountain *et al.*, 2010a, b). The global wavelet power spectrum was calculated for each line down the length of the image. For illustration, two example cores and 128-row moving averages of the vertical variation in μ and σ are shown in Fig. 11A and B. There is redundancy of information in such an approach, and a moving average could smooth over important grain-size transitions. However, for the present purpose, it clearly demonstrates the changes in core texture discernible by eye, and the reported grain sizes are in accord with visual estimates.

Images of non-sedimentary materials

The method is also suitable for other (non-sedimentary) natural patterns which are 'granular' or composed of tessellating elements which possess a distribution of sizes. For example, Eq. 4 was computed for images of: (i) polygonal patterned

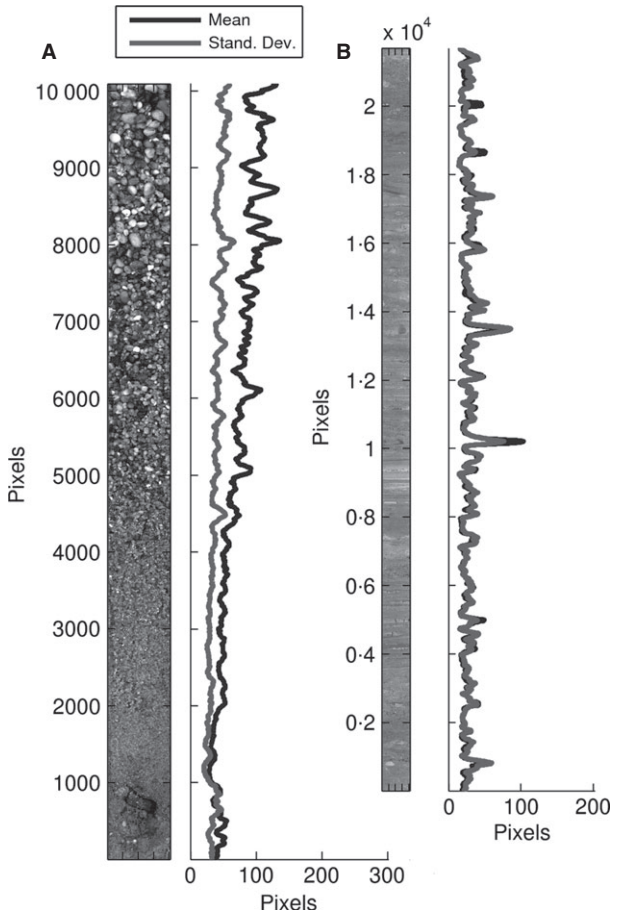

Fig. 11. (A) Left: scan of a 75 cm section of core 014H from expedition 313, site 27, hole A. (B) Left: Scan of a 148 cm section of core 161R from expedition 313, site 28, hole A. Grain-size arithmetic mean (μ, dark lines) and standard deviation (σ, light lines) have been computed per line of pixels and then smoothed using a 128-row moving average to discern the trend.

ground (Fig. 12A to C); (ii) a type of granular sea ice called 'pancake ice' (Fig. 12D to F); and (iii) dried and cracked earth (Fig. 12G to I). In each of these images, the pattern depicted possesses a bi-modal or multi-modal element size distribution. For each image, the global wavelet power spectrum shows clear peaks associated with the wavelengths of features visible by eye.

SENSITIVITY ANALYSES

This section further explores the sensitivities and limitations of the wavelet technique using plan-form simulations of sediments. Simulated sediments have been shown by Buscombe *et al.* (2010) and Buscombe & Rubin (2012b) to be an adequate means by which to explore the sensitivities of automated grain-size algorithms, allowing the control of some sediment attributes whilst testing for others. The effects of preferred grain orientation, and correlation with grain shade (colour) and size are explored.

Effect of anisotropy

Natural sediments are sometimes found with a preferred orientation, particularly those worked by unidirectional flows of water and/or ice where the long axis points in the direction of the flow. Many examples can be found in glacial tills and imbricated river and beach gravels, and many more in the sedimentary record. It is even possible that images of sediment which resolve individual grains might cover sufficient area for the preferential orientation of grains to be both evident and significantly affect grain-size estimates using statistical techniques such as here.

The effect of anisotropy on the algorithm was tested using simulated images consisting of binary ellipses at a preferred orientation. The ellipses were log-normally distributed ($\mu = 1$, $\sigma = 1$) and each had a longest axis twice the length of the shortest axis. Simulations were performed in which grains were oriented 0°, 45° and 315° to the top of the image (respectively, pointing up, towards the top right or towards the top left). The resulting set of images has near-identical grain-size distributions and void fractions. Only the grain orientation differs between images. The method given by Eq. 4 was applied, as before, using a selection (approximately half) of rows and columns from each of the images. As illustrated by Fig. 13, which shows the measured and estimated grain-size distributions overlying the respective simulated images, the orientation of the grains had no significant impact on the grain-size estimates.

Effect of correlation of grain colour and scale

In natural sediment samples, there can be a correlation of grain colour and grain size. Such situations can arise in a mature sediment, for example, if grains of different mineralogies weather and abrade at different rates, or if the sediment is a mixture of populations of grains with different maturities brought together by mixed transport processes. If grain size and shading intensity were positively correlated (larger grains were systematically brighter) one

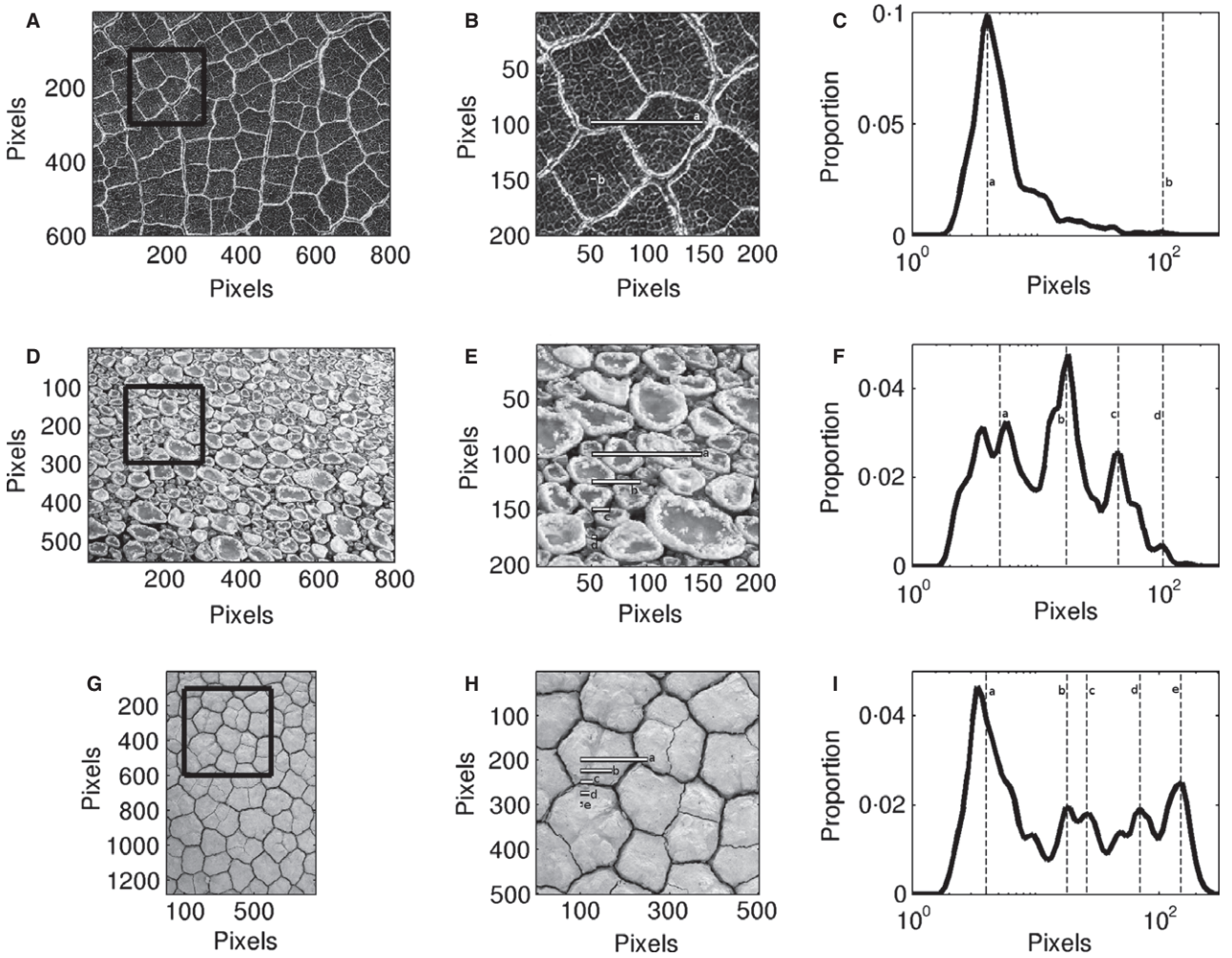

Fig. 12. Images of some naturally occurring non-sedimentary granular patterns: (A) polygonal patterned ground on Mars (NASA/JPL/University of Arizona: Image ESP_016641_2500, RGB non-map projected image); (D) pancake ice; and (G) cracked earth. The portions of the image in each of the boxes are shown in (B), (E) and (H), respectively. The line lengths in each of these close-ups correspond to the scales marked by the vertical dashed lines in the corresponding global wavelet spectra of the images in (A), (D) and (G), shown in (C), (F) and (I), respectively.

might hypothesize that the effect on the wavelet method would be, in general, to over-estimate grain size because greater spectral power would be associated with the larger wavelengths in the image. If larger grains were systematically darker one might expect the opposite situation to be true. To investigate how sensitive the technique is to a correlation between grain shade and size, simulations were used where such a correlation could be artificially imposed and varied.

Simulated sediments composed of randomly oriented log-normally distributed ellipses (where the major axis was exactly twice the minor axis) were once again used. Two sets of images with identical geometric structure were generated. Each set varied the void fraction but the particle size distribution remained constant. In the first set, each grain was shaded randomly so particle size and shade were uncorrelated. In the second set of images, particles were shaded according to eight discrete size classes based on the cumulative size distribution $C(d)$ [namely, $C(d) \leq 0{\cdot}05$, $0{\cdot}05 < C(d) \leq 0{\cdot}1$, $0{\cdot}1 < C(d) \leq 0{\cdot}25$, $0{\cdot}25 < C(d) \leq 0{\cdot}5$, $0{\cdot}5 < C(d) \leq 0{\cdot}75$, $0{\cdot}75 < C(d) \leq 0{\cdot}9$, $0{\cdot}9 < C(d) \leq 0{\cdot}95$ and $C(d) > 0{\cdot}95$]. Importantly, shading intensity (brightness) increased linearly with these grain-size bins. Grain-size distributions were estimated for both sets of images, once again using Eq. 4.

Results for end-member porosities in both sets are shown in Fig. 14: on the left is the sediment image with grains randomly shaded and on the left is the shade correlated with size. As in

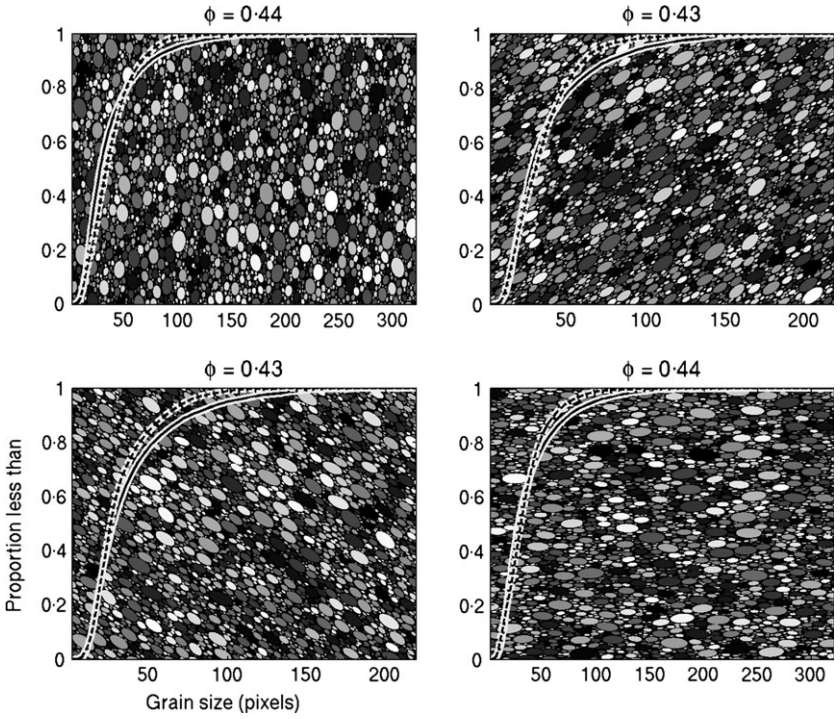

Fig. 13. Simulated two-phase media (shaded areas are particles, black areas are void spaces) consisting of ellipses (the major axis is always twice the minor axis length) with a preferred orientation, along with their known particle size distributions (continuous lines) and estimated size distributions (dashed lines). In each subplot, the horizontal axis is grain size in pixels and the vertical axis is proportion less than. The title of each subplot is the void fraction of the simulation underneath.

Table 7. Percent error in aggregated percentile estimates for idealized log-normally distributed ellipses. Values have been normalized by the particle size associated with that percentile and multiplied by 100 to give a percent error. Values outside of parentheses are for grains randomly shaded. Values inside parentheses are for grains shaded according to their size.

Percentile	P_{10}	P_{16}	P_{25}	P_{50}	P_{75}	P_{84}
Ψ	29 (73)	29 (71)	29 (69)	23 (55)	11 (28)	9 (16)
M	25 (71)	26 (70)	26 (68)	20 (53)	9 (25)	8 (12)
e_i	14 (12)	13 (12)	12 (13)	11 (14)	5 (12)	5 (9)

previous figures, the solid and dashed lines are, respectively, measured and estimated cumulative particle size distributions. Table 7 contains a full summary of errors for both sets of images. As expected, having a situation where grain size and shade are correlated clearly introduces greater error for all percentiles of the size distribution. The general effect is to cause over-prediction of grain size, because grain size and intensity were positively correlated. The irreducible random errors are similar, however, because most of the RMS error in the cases where particle shade and size are correlated is caused by a bias, whereby grain sizes are consistently over-predicted.

DISCUSSION

The present algorithm takes a representative number of rows and columns from each image, computes the global wavelet spectrum from each, then averages the global spectrum from each to provide the grain-size distribution. It is important that both rows and columns are used to mitigate potential issues with grain anisotropy. In the present study, every second or third row and column were used, and the results were satisfactory. However, what constitutes a 'representative' number is yet to be defined precisely. Qualitatively, it would be the point where the new information of an additional row or column

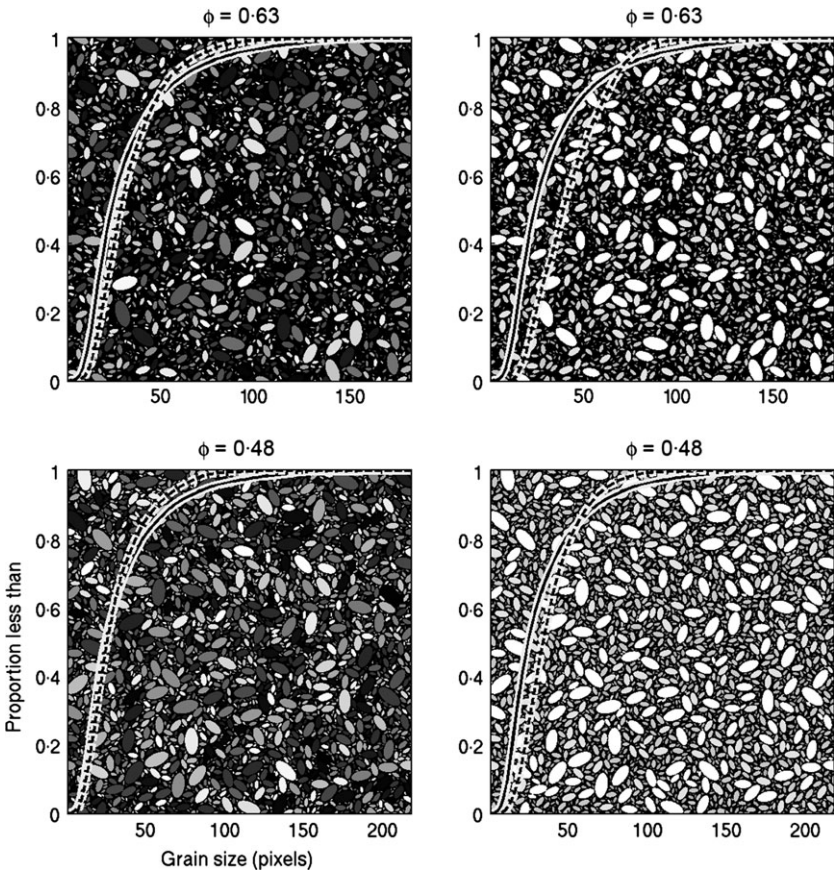

Fig. 14. Simulated two-phase media (shaded areas are particles, black areas are void spaces) consisting of randomly oriented ellipses with a log-normal size distribution, along with their known particle size distributions (continuous lines) and estimated size distributions (dashed lines). In each subplot, the horizontal axis is grain size in pixels and the vertical axis is proportion less than. The title of each subplot is the void fraction of the simulation underneath. The pair of images on each row shows the same sediment bed with different shading of particles. In the left subplot, the grains are shaded randomly (no correlation between shade and size), whereas in the right subplot, the grains are shaded according to their size (shading and size are correlated). Error statistics for these samples are presented in Table 7.

of data either does not significantly change the overall size distribution, and/or does not improve the observation–estimation mismatch. Clearly, further work would be required to ascertain this. Subsequent research would be required to ascertain what minimum sample density is required for a given level of accuracy in the grain-size estimate. This would depend on many factors, such as the degree of homogeneity in the image, any correlation between grain size and shading intensity, and even possible grain shape effects which have not been explored here.

This new wavelet technique deals much better with non-stationarity (non-homogeneous images) compared to previous techniques based on the Fourier-derived spectrum (Buscombe *et al.*, 2010; Buscombe & Rubin, 2012b), as evidenced by the skill of the method for the samples with very few individual grains (set C; Fig. 9) and the two-phase (binary) simulations which also contain relatively few grains (Figs 2, 3, 13 and 14). Fourier-derived spectra of sediment images (for example, Fig. 1E) do not possess sharp peaks at discrete frequencies because a range of frequencies is required to describe the quasi-periodic, non-sinusoidal features in the data (for example, Fig. 1B). Wavelet spectra of the same images often possess an even greater spectral smoothness, due in part to the number of peaks of the mother wavelet in the spatial domain [here, the Morlet mother wavelet used has six peaks in the spatial domain – see Torrence & Compo (1998)] and also the averaging of both spectral and spatial components of the signal.

The difference between the 'geometrical' and 'statistical' approach to grain size from images of sediment is essentially the same as the Nikora & Goring (2004) classification of quantitative

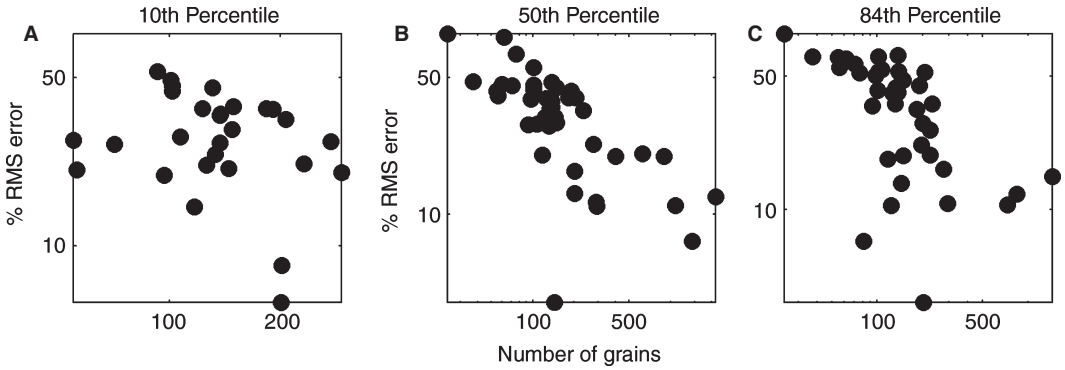

Fig. 15. Root mean square (RMS) % error versus number of individual grains per image for the: (A) 10th, (B) 50th and (C) 84th percentiles of the grain-size distributions. Images come from sets A (Figure 4) and C (Figure 6). As a rule of thumb, a sample size of at least 250 grains per image is required to achieve a RMS error of around 20% or less.

characterization of surface topography into 'discrete' and 'continuous'. The discrete approach identifies individual morphological features, such as ridges, valleys, craters and dunes, based on their geometries, whereas the continuous approach quantifies the salient statistical features of the surface using spectra (e.g. Taylor Perron *et al.*, 2008) and other statistical measures (variograms and structure functions) on both grain-scale (e.g. Aberle & Nikora, 2006; Brassington *et al.*, 2012) and landscape-scale (e.g. Dodds & Rothman, 2000; Stepinski *et al.*, 2002; Nikora & Goring, 2004; Taylor Perron *et al.*, 2008) topographic data sets. The same classification might be used for sediment surfaces, and indeed the techniques employed are similar because both images of sediment and digital elevation models of landscapes are continuous random surfaces (of intensity or elevation, respectively).

The continuous wavelet transform provides a powerful means by which to quantify multiple scales of persistence/autocorrelation from continuous random fields. Highlighting once again the close parallels to statistical characterization of topographic data sets, in combining the benefits of statistical and deterministic approaches, wavelet transforms have been used to characterize surface elevations at a range of scales and environments (e.g. Little *et al.*, 1993; Malamud & Turcotte, 2001; Lashermes *et al.*, 2007). Satellite imagery and topographic data sets from LIDAR and multi-beam acoustics might, in the future, provide the required coverage and spatial resolution so that scales from the individual grain to bedform to interfluve might be uncovered with a single analysis technique. The continuous wavelet transform would be a good candidate for such a multi-scalar scale analysis, especially useful in situations where it is advantageous to relax the strict stationarity requirement of Fourier-based methods, and where both spectral and spatial information is important.

As with all previous methods for grain-size analysis from images of sediment surfaces (both statistical and geometrical), what is actually quantified is the size of apparent axes of grains. In other words, in the image plane where many grains may be overlapping and therefore their axial dimensions are partially obscured. In some situations, this is precisely the information which is required, for example in studies of hydrodynamics and sediment transport because it is this top surface which is interacting with the flow in the form of surface roughness, and seeding the flow with suspended sediments. In other situations, the apparent grain-size distribution needs to be converted to a bulk sample size distribution. The reader is referred to Kellerhals & Bray (1971) and Graham *et al.* (2010, 2012) for a comprehensive review of these phenomena, as well as conversion procedures which are applicable for grain-size distribution measurements from geometrical algorithms such as Graham *et al.* (2005).

In the present technique [indeed by the definition of Buscombe *et al.* (2010) all 'statistical' techniques] the grain size is inferred indirectly, without measuring individual grains. This offers distinct advantages over geometrical approaches, for example it means that it is not subject to the accumulation or errors associated with over-segmenting and under-segmenting grains, which means the same algorithm can be applied across the sedimentary size-spectrum as long as the grains are resolved. The main disadvantage, however, is that whereas in the geometrical

approach, the images can be used to obtain many metrics of grain sizes (including major and minor axes, equivalent circular diameters, etc.), in the present method, the reported grain size is equivalent to the distribution of intermediate apparent axis diameters, and this is the only grain-size metric obtained by the analyses of the present paper (although there should be no theoretical limits on what other measures of grain size are obtained by similar analyses). Different physical and ecological applications of grain-size data require different measures of 'size', which will remain a potential limitation of the statistical approach until modifications or suitable conversions are developed.

SOME PRACTICAL GUIDELINES WHEN USING THIS METHOD

Analysis of sets A and C revealed that root mean square (RMS) error is found to go inversely with sample size (number of grains per image), for all percentiles of the distribution (Fig. 15). Therefore, sampling strategies should be designed such that the area of the photograph is maximized without having a deleterious effect on resolution, to maximize the number of grains within the image.

The errors presented in this manuscript are those of the estimate versus a point count from the same image. Errors are likely to be different when compared to another form of particle size analysis, such as sieving or laser diffraction (Barnard *et al.*, 2007; Warrick *et al.*, 2009). In such cases, a correction must be applied, which will most probably depend on the nature of the sedimentological population. Errors might be further reduced if multiple samples are taken and the results averaged (Barnard *et al.*, 2007; Gallagher *et al.*, 2011). Some recommendations for suitable sediment imagery have already been made by others (Rubin *et al.*, 2007; Warrick *et al.*, 2009; Buscombe *et al.*, 2010; Baptista *et al.*, 2012), so only the most important guidelines for taking suitable sediment imagery will be repeated here. The 'golden rule' is that the individual grains are resolvable by eye. If the smallest grains are less than a few pixels in scale, the present method, or the methods of Rubin (2004), Warrick *et al.* (2009), Buscombe *et al.* (2010) or Buscombe & Rubin (2012b), will not work. In the case of sub-pixel imagery, the reader is referred to the techniques of Carbonneau *et al.* (2004, 2005), Verdu *et al.* (2005) and Dugdale *et al.* (2010) which are designed for under-resolved imagery (for example, from aerial and satellite platforms).

Ideally, the image should be of the sediment surface in planform so no orthorectification is required, and ideally the image should not contain non-sedimentary material, such as vegetation and other organic matter larger than the grain scale. If such material is present, if the image covers a sufficient area, it can be sub-sampled (cropped) so as to avoid non-sedimentary material and the analyses performed on each sub-sample. For guidelines concerning large shadows and partially wet sediment, the reader is referred to, respectively, Buscombe *et al.* (2010) and Warrick *et al.* (2009) for some guidance.

As shown above, the method is relatively insensitive to grain orientation (Fig. 13), yet sensitive to situations where grain shade is correlated with grain size (Fig. 14), so care should be taken in such circumstances to correct for the bias that this introduces. It has also been shown that errors increase if insufficient numbers of grains are present. At least a few hundred grains must be present for a reliable grain-size estimate, and preferably thousands (providing that the grains are well-resolved), particularly if the sediment is not well-sorted. In general, if there is a compromise to be made between the typical number of grains in the image and grain resolution, a rule of thumb is that it is almost always preferable to have fewer well-resolved grains than lots of under-resolved grains.

The colour information in the image is not used by the method, only grey-scale (8-bit) intensities. In most of the sediment images collected by the author, in a wide range of sediment environments, there is almost always a sufficiently wide range of grain shades in intensity images. If, however, all the grains have very similar intensities in a grey-scale image, such as in images of coral sands or volcanic glass sands, this can potentially lead to problems, and an imaging capability which yields a larger contrast must be sought. A couple of such images are shown in Fig. 10 (top left and middle bottom) for reference.

CONCLUSIONS

Previously described automated methods for estimating the grain-size distribution from an image of sedimentary material rely on either: complicated image processing (segmentation of individual grains; e.g. Chang & Chung, 2012);

calibration (e.g. Rubin, 2004; Warrick *et al.*, 2009); relatively well-sorted samples; or a relatively large number of grains (e.g. Buscombe *et al.*, 2010; Buscombe & Rubin, 2012b). Here, a method is proposed which circumnavigates these issues. The complete size distribution of apparent grain axes in an image of sediment is well-approximated by the global wavelet power spectrum. The grain-size distribution obtained is equivalent to the distribution of apparent intermediate grain diameters, grid by number style. No image filtering or other processing is required. A sample size of around 250 grains per image is required to achieve a root mean square error of around 20% or less. This compares to more than approximately 1000 grains per image for the same level of accuracy for a similar method based on the Fourier-derived spectrum (Buscombe *et al.*, 2010).

This new method was tested using 300 images from 46 populations of unconsolidated sands and gravels from diverse sedimentary environments, nine thin sections through different sedimentary rock types, long marine sediment cores and other types of natural patterns composed of tessellating elements. The test suite of images therefore displayed considerable variability in origin (biogenic and mineral), size (uni-modal, bi-modal and multi-modal distributions), surface texture and shape. This approach is the first statistical algorithm which provides completely automated, highly accurate grain-size distributions from images of sediment, and which is transferable, in unmodified form, for both consolidated and unconsolidated surface sediments and also some non-sedimentary material. It is suggested that the robustness of the new method is because it efficiently uses both spectral and spatial information from the image, rather than discarding one or the other like previous image-based grain-size techniques. Similar wavelet methods may have applicability for spatial-scale analysis of other continuous random fields in sedimentology, such as topographic data sets.

ACKNOWLEDGEMENTS

Images provided by Dave Rubin and Jon Warrick (US Geological Survey), Rob Holman (Oregon State University), Christoph Heubeck (Freie Universität Berlin) and David McInroy (British Geological Survey). Thanks all. Wavelet computations were based on software developed by C. Torrence and G. Compo. All simulation and grain-size analysis code is freely available from the author upon email request.

REFERENCES

Aberle, J. and **Nikora, V.** (2006) Statistical properties of armoured gravel bed surfaces. *Water Resour. Res.*, **42**, W11414.

Adams, J. (1979) Gravel size analysis from photographs. *ASCE J. Hydraul. Div.*, **105**, 1247–1255.

Baptista, P., **Cunha, T.R.**, **Gama, C.** and **Bernandes, C.** (2012) A new and practical method to obtain grain size measurements in sandy shores based on digital image acquisition and processing. *Sed. Geol.*, **282**, 294–306.

Barnard, P., **Rubin, D.M.**, **Harney, J.** and **Mustain, N.** (2007) Field test comparison of an autocorrelation technique for determining grain size using a digital 'beachball' camera versus traditional methods. *Sed. Geol.*, **201**, 180–195.

Brassington, J., **Vericat, D.** and **Rychkov, I.** (2012) Modelling river bed morphology, roughness and surface sedimentology using high-resolution terrestrial laser scanning. *Water Resour. Res.*, **48**, W11519.

Buscombe, D. (2008) Estimation of grain size-distributions and associated parameters from digital images of sediment. *Sed. Geol.*, **210**, 1–10.

Buscombe, D. and **Masselink, G.** (2009) Grain size information from the statistical properties of digital images of sediment. *Sedimentology*, **56**, 421–438.

Buscombe, D. and **Rubin, D.M.** (2012a) Advances in the simulation and automated measurement of well sorted granular material. Part 1: simulations. *J. Geophys. Res.*, **117**, F02001.

Buscombe, D. and **Rubin, D.M.** (2012b) Advances in the simulation and automated measurement of well sorted granular material. Part 2: direct measures of particle properties. *J. Geophys. Res.*, **117**, F02002.

Buscombe, D., **Rubin, D.M.** and **Warrick, J.A.** (2010) A universal approximation to grain size from images of non-cohesive sediment. *J. Geophys. Res.*, **115**, F02015.

Butler, J.B., **Lane, S.N.** and **Chandler, J.H.** (2001) Automated extraction of grain-size from gravel surfaces using digital image processing. *J. Hydraul. Res.*, **39**, 519–529.

Carbonneau, P., **Lane, S.N.** and **Bergeron, N.** (2004) Catchment-scale mapping of surface grain size in gravel bed rivers using airborne digital imagery. *Water Resour. Res.*, **40**, W07202.

Carbonneau, P., **Bergeron, N.** and **Lane, S.** (2005) Automated grain size measurements from airborne remote sensing for long profile measurement of fluvial grain sizes. *Water Resour. Res.*, **41**, W11426.

Chang, F.-J. and **Chung, C.-H.** (2012) Estimation of riverbed grain-size distribution using image-processing techniques. *J. Hydrol.*, **440–441**, 102–112.

Dodds, P.S. and **Rothman, D.H.** (2000) Scaling, universality and geomorphology. *Annu. Rev. Earth Planet. Sci.*, **28**, 571–610.

Dugdale, S., **Carbonneau, P.** and **Campbell, D.** (2010) Aerial photosieving of exposed gravel bars for the rapid calibration of airborne grain size maps. *Earth Surf. Proc. Land.*, **35**, 627–639.

Duller, R.A., **Whittaker, A.C.**, **Fedele, J.J.**, **Whitchurch, A.L.**, **Springett, J.**, **Allen, P.A.**, **Smithells, R.A.** and **Fordyce, S.**

(2010) From grain size to tectonics. *J. Geophys. Res.*, **112**, F01002.

Farge, M. (1992) Wavelet transforms and their applications to turbulence. *Annu. Rev. Fluid Mech.*, **24**, 395–457.

Gaillot, P., **Darrozes, J.** and **Bouchez, J.-L.** (1999) Wavelet transform: a future of rock fabric analysis? *J. Struct. Geol.*, **21**, 1615–1621.

Gallagher, E.L., **MacMahan, J.**, **Reniers, A.J.H.M.**, **Brown, J.** and **Thornton, E.B.** (2011) Grain size variability on a rip-channeled beach. *Mar. Geol.*, **287**, 43–53.

Graham, D.J., **Reid, I.** and **Rice, S.** (2005) Automated sizing of coarse-grained sediments: image processing procedures. *Math. Geol.*, **37**, 1–28.

Graham, D.J., **Rollet, A.-J.**, **Piegay, H.** and **Rice, S.** (2010) Maximizing the accuracy of image-based surface sediment sampling techniques. *Water Resour. Res.*, **46**, W02508.

Graham, D.J., **Rollet, A.-J.**, **Rice, S.** and **Piegay, H.** (2012) Conversions of surface grain-size samples collected and recorded using different procedures. *J. Hydraul. Eng.*, **138**, 839–849.

Grinsted, A., **Moore, J.C.** and **Jevrejeva, S.** (2004) Application of the cross wavelet transform and wavelet coherence to geophysical time series. *Nonlinear Process. Geophys.*, **11**, 561–566.

Ibbeken, H. and **Schleyer, R.** (1986) Photo-sieving: a method for grain-size analysis of coarse-grained, unconsolidated bedding surfaces. *Earth Surf. Proc. Land.*, **11**, 59–77.

Kellerhals, R. and **Bray, D.I.** (1971) Sampling procedures for coarse fluvial sediments. *ASCE J. Hydraul. Div.*, **97**, 1165–1179.

Laine, A. and **Fan, J.** (1993) Texture classification by wavelet packet signatures. *IEEE Trans. Pattern Anal. Mach. Intell.*, **15**, 1186–1191.

Lashermes, B., **Foufoula-Georgiou, E.** and **Dietrich, W.E.** (2007) Channel network extraction from high resolution topography using wavelets. *Geophys. Res. Lett.*, **34**, L23S04.

Little, S.A., **Carter, P.H.** and **Smith, D.K.** (1993) Wavelet analysis of a bathymetric profile reveals an anomalous crust. *Geophys. Res. Lett.*, **20**, 1915–1918.

Malamud, B.D. and **Turcotte, D.L.** (2001) Wavelet analyses of Mars polar topography. *J. Geophys. Res.*, **106**, 17497–17504.

Mao, L., **Cooper, J.R.** and **Frostick, L.E.** (2011) Grain size and topographical differences between static and mobile armour layers. *Earth Surf. Proc. Land.*, **36**, 1321–1334.

Mountain, G.S., **Proust, J.**, **McInroy, D.**, **Cotterill, C.**, *et al.* (2010a) Visual core description and core images of hole 313-m0027a. *Proc. Integrated ODP*, **313**. doi:10.2204/iodp.proc.313.2010.

Mountain, G.S., **Proust, J.**, **McInroy, D.**, **Cotterill, C.**, *et al.* (2010b) Visual core description and core images of hole 313-m0028a. *Proc. Integrated ODP*, **313**. doi:10.2204/iodp.proc.313.2010.

Nelson, P.A., **Bellugi, D.** and **Dietrich, W.E.** (2012) Delineation of river bed-surface patches by clustering high-resolution spatial grain size data. *Geomorphology*. in press, doi: 10.1016/j.geomorph.2012.06.0n08.

Nikora, V. and **Goring, D.** (2004) Mars topography: bulk statistics and spectral scaling. *Chaos, Solitons Fractals*, **19**, 427–439.

Paola, C. and **Seal, R.** (1995) Grain size patchiness as a cause for selective deposition and downstream fining. *Water Resour. Res.*, **31**, 1395–1408.

Percival, D.P. (1995) On estimation of the wavelet variance. *Biometrika*, **82**, 619–631.

Qi, X. and **Neupauer, R.** (2008) Wavelet analysis of dominant scales of heterogeneous porous media. *Water Resour. Res.*, **44**, W09406.

Qi, X. and **Neupauer, R.** (2010) Wavelet analysis of characteristic length scales and orientation of two-dimensional heterogeneous porous media. *Adv. Water Resour.*, **33**, 514–524.

Rubin, D.M. (2004) A simple autocorrelation algorithm for determining grain size from digital images of sediment. *J. Sediment. Res.*, **74**, 160–165.

Rubin, D.M., **Chezar, H.**, **Harney, J.N.**, **Topping, D.J.**, **Melis, T.S.** and **Sherwood, C.R.** (2007) Underwater microscope for measuring spatial and temporal changes in bed-sediment grain size. *Sed. Geol.*, **202**, 402–408.

Stepinski, T.F., **Marinova, M.M.**, **McGovern, P.J.** and **Clifford, S.M.** (2002) Fractal analysis of drainage basins on Mars. *Geophys. Res. Lett.*, **29**, 1189.

Taylor Perron, J., **Kirchner, J.W.** and **Dietrich, W.E.** (2008) Spectral signatures of characteristic spatial scales and nonfractal structure in landscapes. *J. Geophys. Res.*, **113**, F04003.

Torrence, C. and **Compo, G.** (1998) A practical guide to wavelet analysis. *Bull. Am. Meteorol. Soc.*, **79**, 61–78.

Tschopp, M.A., **Wilks, G.B.** and **Spowart, J.E.** (2008) Multi-scale characterization of orthotropic microstructures. *Modell. Simul. Mater. Sci. Eng.*, **16**, 065009.

Verdu, J.M., **Batalla, R.J.** and **Martinez-Casasnovas, J.A.** (2005) High-resolution grain-size characterisation of gravel bars using imagery analysis and geo-statistics. *Geomorphology*, **72**, 73–93.

Warrick, J.A., **Rubin, D.M.**, **Ruggiero, P.**, **Harney, J.**, **Draut, A.E.** and **Buscombe, D.** (2009) Cobble cam: grain-size measurements of sand to boulder from digital photographs and autocorrelation analyses. *Earth Surf. Proc. Land.*, **34**, 1811–1821.

Whittaker, A.C., **Duller, R.A.**, **Springett, J.**, **Smithells, R.A.**, **Whitchurch, A.L.** and **Allen, P.A.** (2011) Decoding downstream trends in stratigraphic grain size as a function of tectonic subsidence and sediment supply. *GSA Bull.*, **123**, 1363–1382.

Manuscript received 25 November 2012; revision accepted 14 March 2013